



Evidence accumulation during perceptual decisions in humans varies as a function of dorsal frontoparietal organization

Méadhbh B. Brosnan^{1,2} , Kristina Sabaroedin^{1,2} , Tim Silk^{3,4,5}, Sila Genc^{3,5}, Daniel P. Newman^{1,2}, Gerard M. Loughnane⁶, Alex Fornito^{1,2,7}, Redmond G. O'Connell^{1,2,8,9} and Mark A. Bellgrove^{1,2,8,9}

Animal neurophysiological studies have identified neural signals within dorsal frontoparietal areas that trace a perceptual decision by accumulating sensory evidence over time and trigger action upon reaching a threshold. Although analogous accumulation-to-bound signals are identifiable on extracranial human electroencephalography, their cortical origins remain unknown. Here neural metrics of human evidence accumulation, predictive of the speed of perceptual reports, were isolated using electroencephalography and related to dorsal frontoparietal network (dFPN) connectivity using diffusion and resting-state functional magnetic resonance imaging. The build-up rate of evidence accumulation mediated the relationship between the white matter macrostructure of dFPN pathways and the efficiency of perceptual reports. This association between steeper build-up rates of evidence accumulation and the dFPN was recapitulated in the resting-state networks. Stronger connectivity between dFPN regions is thus associated with faster evidence accumulation and speeded perceptual decisions. Our findings identify an integrated network for perceptual decisions that may be targeted for neurorehabilitation in cognitive disorders.

Greater error rates and increased trial-to-trial variability in response times are ubiquitous findings across a range of cognitive operations in clinical disorders such as Parkinson's disease, schizophrenia and attention deficit hyperactivity disorder (ADHD)^{1–3}. Recent work has attempted to reconcile these disparate deficits within integrated, computational models. One class of computational modelling that has gained traction in psychological research is sequential sampling. Such models (such as the drift diffusion model) assume that sensory evidence is sampled and accumulated to inform perceptual decisions^{4,5}. Parameters of these models have utility in explaining classic psychological phenomena, such as the speed–accuracy trade-off effect, as well as cognitive impairments in healthy aging and cognitive disorders (for example, refs. ^{6,7}). Despite their explanatory power, these models provide little insight into the underlying neural circuits that mediate these deficiencies. Yet, an understanding of the neural circuits mediating perceptual decision-making could have great utility in identifying targets for neurorehabilitation in clinical disorders.

Parallel, invasive electrophysiology work in monkeys and rodents has identified neural signals that trace a decision variable by accumulating sensory evidence over time and trigger action upon reaching a threshold^{8–10}. These decision variables tracking evidence accumulation are observable throughout the cortical hierarchy, including the midbrain^{11,12}, premotor regions¹³, primary motor cortex¹⁴ and within the frontoparietal network (FPN^{15,16}). Behavioural manipulations, such as prioritizing the speed over accuracy of perceptual reports, are associated with altered evidence

accumulation signals within several distinct areas of the dorsal FPN (dFPN), including the lateral intraparietal cortex¹⁷, frontal eye fields (FEFs)¹⁸ and premotor cortex¹⁹. These findings indicate a pivotal contribution of these brain areas to the speed of perceptual reports. The presence of evidence accumulation signals in separate dFPN areas that evolve across very similar timescales raises the question of whether communication between these areas is critical for successful perceptual decision-making.

In humans, unprecedented access into the temporal dynamics of the neurophysiology of perceptual decisions has been gained through recent advances in both model design and analysis techniques^{20–22}. Using techniques such as electroencephalography (EEG) and magneto-encephalography, this work has enabled the isolation of neural decision signals in humans that are analogous to those observed in other animals^{20,21,23–26}. The centro-parietal positivity (CPP) is a neural signal recorded with a human electroencephalogram (EEG) that bares remarkable similarities to invasive electrophysiological markers of evidence accumulation^{4,20}. Specifically, it builds during decision formation in accordance with sensory evidence strength, triggers action upon reaching a decision threshold, predicts the timing and accuracy of perceptual reports, and demonstrates amplitude modulations in a manner consistent with decision-bound adjustments^{4,20,22,25,27}. It is supramodal, distinguishable from early stimulus selection²⁵ and fully independent of motor response requirements (effector independent); it is present whether or not a motor response is required and irrespective of whether an action is required immediately, or at a later time point^{4,5}. When a

¹Turner Institute for Brain and Mental Health, Monash University, Melbourne, Victoria, Australia. ²School of Psychological Sciences, Monash University, Melbourne, Victoria, Australia. ³Developmental Imaging, Murdoch Children's Research Institute, The Royal Children's Hospital, Melbourne, Victoria, Australia. ⁴Cognitive Neuroscience Unit, School of Psychology, Deakin University, Geelong, Victoria, Australia. ⁵Department of Paediatrics, University of Melbourne, Melbourne, Victoria, Australia. ⁶School of Business, National College of Ireland, Dublin, Ireland. ⁷Brain and Mental Health Laboratory, Turner Institute for Brain and Mental Health, Monash University, Melbourne, Victoria, Australia. ⁸Trinity College Institute of Neuroscience, Trinity College Dublin, Dublin, Ireland. ⁹School of Psychology, Trinity College Dublin, Dublin, Ireland. ✉e-mail: brosnanmeadhb@gmail.com; mark.bellgrove@monash.edu

motor action is triggered upon reaching a decision threshold, the CPP precedes motor preparatory signals⁴. As such, this component appears to reflect a distinct and intermediate stage between processing early stimulus information and generating a motor response. That is, the CPP traces the evolution of evidence accumulation in a uniquely abstract manner, triggering action upon reaching a threshold^{4,20}. Accordingly, the CPP has been utilized to extract decision variable information across a vast array of perceptual tasks^{28–32} and modalities^{33,34}, and is strongly associated with individuals' subjective perceptual experience³⁵.

In contrast with neurophysiological markers of motor preparatory activity, such as oscillatory changes within Mu and beta frequency bands, whose cortical origins are well established (for example, ref. ³⁶), structural underpinnings of the CPP remain elusive. Perceptual decision formation and the dynamics of the CPP (including onset latency, build-up rate and amplitude) are influenced by inter-related processes including levels of attentional engagement⁴, and the efficacy of target selection²⁵, which render it difficult to isolate cortical regions specifically relating to evidence accumulation. In addition, the speed of perceptual reports varies with post-evidence accumulation processes such as motor preparation and execution²⁰. Intracranial human electrophysiological recordings and functional magnetic resonance imaging (fMRI) investigations of the P300—an EEG marker that is analogous to the CPP⁵—have highlighted an array of neural sources, including regions of the dFPN^{37,38}. Determining a specific role for the dFPN in human evidence accumulation requires a multi-modal approach that can integrate the temporal dynamics of the CPP with the structural and functional organization of the dFPN.

One anatomical pathway that could provide the mechanism for communication throughout the dFPN is the dorsal branch of the superior longitudinal fasciculus (SLF)—a white matter fronto-parietal association pathway with projections to the intraparietal sulcus (IPS); the human homologue to the monkey lateral intraparietal cortex), FEF and premotor cortex³⁹. The regions connected with the dorsal SLF comprise the so-called dorsal attention network (herein referred to as the dFPN), which often shows coherent activity both at rest and during task activation, and is known to underpin goal-directed stimulus processing^{40,41}. Here, we combined MRI and EEG to test the hypothesis that dFPN connectivity underpins the efficiency of perceptual decision formation. First, we leveraged the high temporal resolution of EEG to isolate the CPP as a neural metric of the efficiency of an individual's evidence accumulation process during a variant of the random-dot motion task. Second, we acquired diffusion MRI in the same individuals and tested whether white matter structural organization of the dorsal SLF relates to inter-individual differences in the build-up rate of evidence accumulation and the speed of perceptual reports. Third, resting-state fMRI (rs-fMRI) was acquired in the same individuals to ask whether variability in our neurophysiological and behavioural markers of performance is related to functional connectivity within the dFPN. We present results indicating that evidence accumulation signals predicting the speed of perceptual reports vary according to both structural and functional connectivity within the dFPN.

Results

Neurophysiological markers of evidence accumulation and motor preparation relate to the speed of perceptual reports. First, we sought to validate previous observations of the CPP build-up rate as a reliable neural predictor of the efficiency of perceptual decision formation^{20,22}. A variant of the classic random-dot motion task⁴² was employed to isolate critical neurophysiological dynamics of this evidence accumulation marker, including its onset latency, build-up rate and amplitude²⁰ (Fig. 1). We also measured other neural metrics indexing discrete stages of information processing related to perceptual decisions, including pre-target attentional engagement

(alpha power⁴), early target selection (N2c amplitude and latency²⁵), frontal preparatory activity (frontocentral negativity (FCN); Kelly and O'Connell⁴) and motor preparation (left hemisphere beta; LHB²⁰). For a discussion on using this model to estimate an individual's capacity for evidence accumulation, see Supplementary Results 1 and Extended Data Fig. 1. Participants ($n = 56$; 29 female; mean age: 22.66 years; age range: 18.03–36.92 years) performed the task while EEG data were acquired from 64 electrodes (mean response time: 577.92 ms; range: 437.26–809.96 ms; Fig. 1a; see Methods).

We examined how each neurophysiological marker contributed to the response time, over and above the contributions made by those processes that temporally preceded it, using hierarchical linear regression. A limitation of null hypothesis significant testing is that non-significant P values cannot be interpreted as support for the null hypothesis⁴³. To circumvent this issue and confirm whether the non-significant findings reported represent support for the null hypothesis, we ran Bayes factor analyses. We report the inclusion Bayes factor (BF_{10}) values, whereby values above 1 indicate strength of evidence in favour of the alternative and values below 1 indicate strength of evidence in favour of the null. Age and gender offered no significant improvement in the model fit compared with the intercept-only model (adjusted coefficient of determination (R^2_{adj}) = -0.004 ; $P = 0.42$). Pre-target alpha power ($R^2_{adj} = 0.12$; $R^2_{change} = 0.13$; $P = 0.006$; 95% confidence interval (CI) = 1.13 to 6.23; $BF_{10} = 0.45$; Extended Data Fig. 2 and Supplementary Fig. 1), N2c amplitude ($R^2_{adj} = 0.22$; $R^2_{change} = 0.11$; $P = 0.009$; 95% CI = 1.74 to 11.63; $BF_{10} = 0.53$; Extended Data Fig. 2) and N2c latency ($R^2_{adj} = 0.29$; $R^2_{change} = 0.08$; $P = 0.02$; 95% CI = 0.19 to 1.75; $BF_{10} = 0.25$; Extended Data Fig. 2) significantly improved the model fit for response time. CPP onset latency offered no statistically significant additional improvement in the modelling response time ($R^2_{adj} = 0.3$; $R^2_{change} = 0.02$; $P = 0.2$; 95% CI = -0.39 to 0.08; $BF_{10} = 0.38$). In contrast, the CPP build-up rate significantly improved the model performance, accounting for an additional 10% of the variance ($R^2_{adj} = 0.42$; $R^2_{change} = 0.12$; $P = 0.001$; 95% CI = -657.73 to -167.53 ; $BF_{10} = 200.06$; Fig. 1). Adding CPP amplitude did not alter the model fit ($R^2_{adj} = 0.42$; $R^2_{change} = 0.004$; $P = 0.52$; 95% CI = -2.69 to 1.34; $BF_{10} = 0.34$). Finally, both FCN amplitude ($R^2_{adj} = 0.46$; $R^2_{change} = 0.05$; $P = 0.03$; 95% CI = -3.01 to -0.13 ; $BF_{10} = 0.34$; Extended Data Fig. 2) and stimulus-locked peak LHB latency ($R^2_{adj} = 0.65$; $R^2_{change} = 0.17$; $P < 0.0005$; 95% CI = 0.26 to 0.60; $BF_{10} = 7088.71$; Extended Data Fig. 2) offered significant improvements in the model. For detailed frequentist statistics from this modelling procedure, see Supplementary Table 1.

Second, to isolate signals explaining independent variance in response time, over and above that explained by other signals, all EEG signatures offering significant improvements in the model fit for response time above (that is, pre-target alpha power, N2c amplitude, N2c latency, CPP build-up rate, FCN amplitude and LHB latency) were entered into a single separate linear regression model. When all six independent variables were included in the final model, they accounted for 60.9% of the variation (Cohen's $f^2 = 1.87$) in response time ($F_{6,49} = 15.31$; $P < .0001$; partial $\eta^2 = 0.65$). Only CPP build-up rate and LHB latency were significant independent predictors of behaviour (Fig. 1b,c and Table 1). For an extensive discussion of the potential contribution of the EEG signatures under investigation to perceptual reports, see Supplementary Results 2 and Supplementary Discussion. These data validate previous findings that these neurophysiological signatures of sensory evidence accumulation (CPP) and motor preparation (LHB) account for unique variance in the speed of perceptual reports²⁰.

Defining white matter structural organization of the FPN. The SLF—a network of white matter tracts connecting frontal with parietal regions—is organized into three separate longitudinal pathways: the dorsal (SLF1), middle (SLF2) and ventral (SLF3) branches.

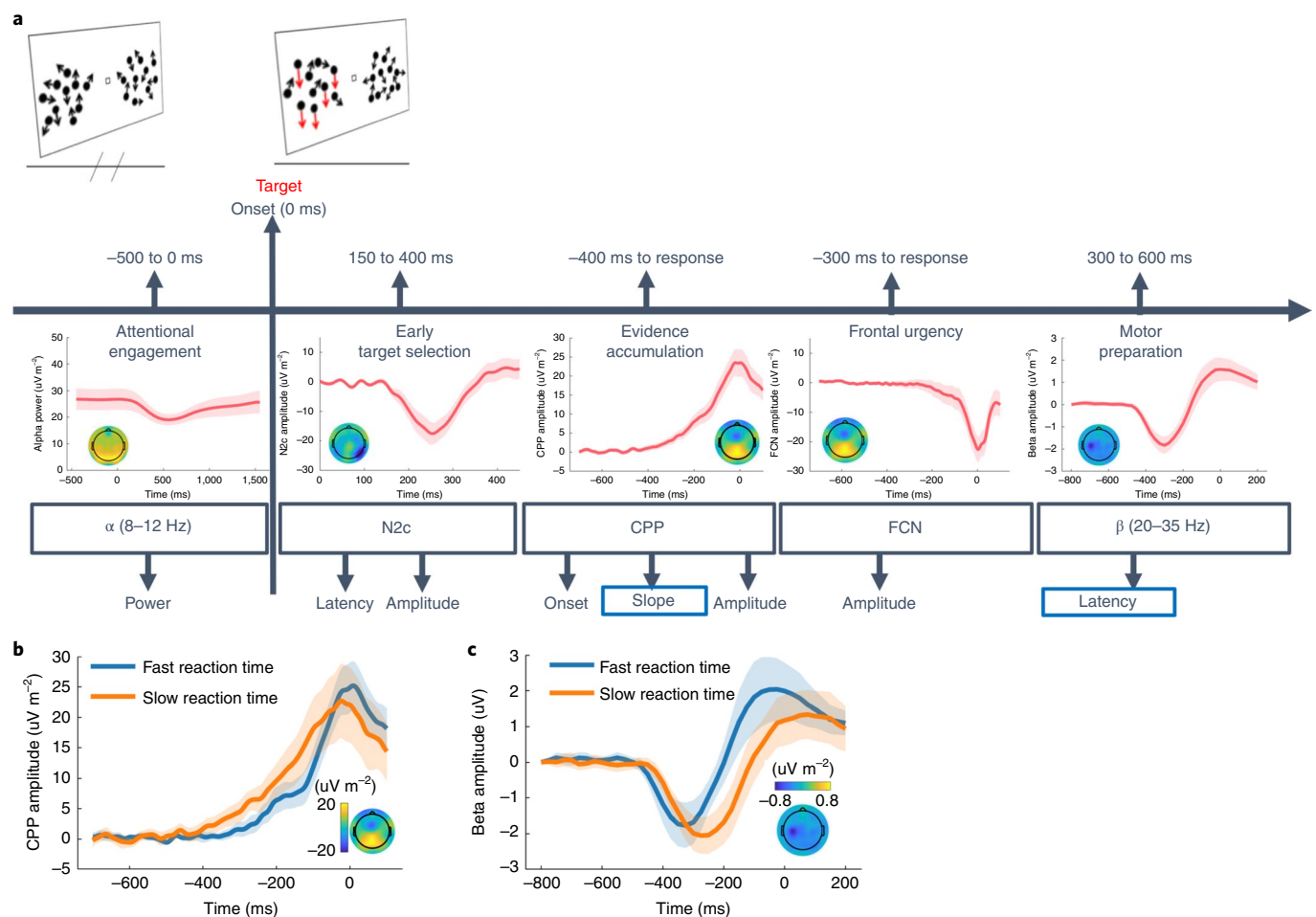


Fig. 1 | Evidence accumulation (CPP build-up rate) and motor preparation (LHB latency) relate to the speed of perceptual reports. a, The combined perceptual decision-making- EEG framework isolating neurophysiological processes contributing to the speed of perceptual reports. During the random-dot motion task, participants fixated centrally while two patches of randomly moving dots were presented peripherally in both hemifields. During target trials, 50% of the dots in one hemifield transitioned from random to coherent motion in a downward direction. Participants' performance was assessed via the speed of perceptual reports, as indicated by a right-hand button press. Eight EEG metrics were extracted to measure the neurophysiological processes. Note that the EEG waveforms represent the grand average signals with confidence intervals ($n = 56$). Topographical distributions of the components are displayed with scales in **c** and in Extended Data Fig. 2. All neurophysiological metrics were modelled as a function of response time. **b,c**, Topoplot scales (see also Supplementary Fig. 2) for CPP build-up rate (**b**; standardized $\beta = -0.39$; $t = -4.29$; $P < .001$; 95% CI = -601.16 to -217.68 ; $BF_{10} = 720.09$) and lateralized beta latency (**c**; standardized $\beta = 0.45$; $t = -4.34$; $P < 0.001$; 95% CI = 0.20 to 0.55 ; $BF_{10} = 6,737.60$), which accounted for independent variance in the response time. Note that the CPP waveform (**b**) is response aligned and the scalp topography plot depicts the distribution of signal across the scalp from -100 ms to the time of response. The beta waveform (**c**) is stimulus aligned and the scalp topography depicts activity from 300 – 700 ms post-target onset. Both signals (**b** and **c**) are binned by response time (using a median split of participants' performance) for visualization purposes only.

Table 1 | Parameter estimates from the final linear regression model for reaction time as a function of the EEG signals

Signal	Standardized β	t	P	95% CI	BF_{10}
Pre-target alpha	0.12	1.19	0.24	-0.81 to 3.16	0.59
N2c amplitude	0.11	1.12	0.27	-0.16 to 5.75	0.69
N2c latency	0.02	0.18	0.86	-0.53 to 0.63	0.34
CPP build-up rate	-0.39	-4.29	<0.0001	-601.16 to -217.68	720.09
FCN amplitude	-0.09	-0.98	0.33	-1.83 to 0.64	0.44
LHB latency	0.45	4.34	$<.0001$	0.20 to 0.55	6,737.60

Evidence accumulation (CPP) build-up rate and motor preparation (LHB) latency exerted partially independent influences on response time. The absolute value of standardized β represents the importance of each predictor, independent of the unit of measurement. CI denotes the CI for β .

SLF1 projects to dFPN areas and we hypothesized that stronger connectivity within this network would facilitate a steeper build-up rate of the CPP. SLF3 projects to regions of the ventral FPN (vFPN), with

SLF2 projecting to both dorsal and ventral networks⁴⁴. Virtual dissection of the three SLF branches was performed using a multiple regions of interest (ROIs) approach⁴⁴ (see Methods). Tract volume

Table 2 | Parameter estimates from the final linear regression model for the dorsal SLF tract as a function of CPP build-up rate

Tract measure	Signal(s)	Standardized β	t	P	95% CI	BF ₁₀
SLF1 volume	CPP build-up rate	0.42	3.35	0.001	0.03 to 0.10	22.26

Standardized β represents the importance of the predictor, independent of the unit of measurement. This model explained 15.7% of the variance in SLF1 volume ($F_{1,54}=11.21$; $P=0.001$; partial $\eta^2=0.17$).

(controlling for whole-brain white matter volume) and mean tract fractional anisotropy were estimated for each branch.

The build-up rate of evidence accumulation relates to macrostructural organization of the dorsal SLF branch. To model inter-individual differences in macro- and microstructural organization (volume and fractional anisotropy, respectively) of the SLF as a function of across-participant differences, the neurophysiological signals, CPP build-up rate and LHB latency (signals accounting for independent variance in the speed of perceptual reports) were entered into separate regression models for each of the three SLF branches. We applied a Bonferroni multiple-comparison correction ($\alpha/12$) accounting for 12 statistical tests (two EEG metrics (CPP build-up rate and LHB latency), three SLF tracts (SLF1, SLF2 and SLF3) and two tract measures (volume and fractional anisotropy)).

CPP build-up rate accounted for independent variance in the model fit for SLF1 volume (standardized $\beta=0.41$; $t=3.1$; $P=0.003$; 95% CI=0.02 to 0.12; BF₁₀=14.54; $F_{2,53}=5.52$; $P=0.007$; partial $\eta^2=0.17$), a result that could not be explained by in-scanner head motion (Supplementary Results 4 and Supplementary Fig. 2). In contrast, there was no statistically significant relationship between LHB latency and SLF1 volume (standardized $\beta=-0.02$; $t=-0.19$; $P=0.85$; 95% CI=0 to 0). We found anecdotal evidence that the data supported the null model over the alternative model with a Bayes factor of 1.79 (BF₁₀=0.56). To obtain accurate parameter estimates for the relationship between CPP build-up rate and SLF1, not influenced by the non-informative LHB latency, CPP build-up rate was entered into a separate linear regression model. This model explained 15.7% of the variance in SLF1 volume (Table 2 and Fig. 2b). To investigate whether the observed association between SLF1 organization and CPP build-up rate could be due to variability of the evidence accumulation processes, we computed CPP variability across trials (Supplementary Results 3). There was no statistically significant relationship between this measure and SLF1 organization and we observed that the data supported the null model over the alternative model with a Bayes factor of 3.45, indicating that SLF1 specifically relates to the efficiency, and not the consistency, of the evidence accumulation process.

Adding CPP build-up rate or LHB latency did not improve the model fit for SLF2 or SLF3 volume (SLF2 volume: $R^2_{\text{adj}} < -0.01$; both $P > 0.24$; SLF3 volume: $R^2_{\text{adj}} < -0.03$; both $P > 0.44$) and the data supported the null model over the alternative model in all cases with a Bayes factor of at least 2.78 (all BF₁₀ < 0.36; see Supplementary Tables 1 and 2 for detailed Bayesian and frequentist results). These findings show that the relationship between the SLF and evidence accumulation build-up rate is specific to the most dorsal branch of the tract (Fig. 2b). There was no statistically significant association between either CPP build-up rate or LHB latency with microstructural properties (mean fractional anisotropy) of any SLF branches (all $R^2_{\text{adj}} < -0.02$; all $P > 0.28$; all BF₁₀ < 0.41).

The build-up rate of evidence accumulation mediates the relationship between the dorsal SLF volume and the speed of perceptual reports. The results thus far show that a larger SLF1 volume is associated with a faster build-up rate (slope) of the CPP (Fig. 2c), and that the CPP build-up rate is independently associated with response time (Fig. 1c). These findings suggest that the dorsal SLF may represent an anatomical constraint on the speed of perceptual reports. We therefore tested whether the CPP build-up rate mediated

the relationship between SLF1 volume and response time^{45,46}. Bootstrapped mediation analysis (5,000 samples) confirmed that this was indeed the case (indirect effect: $-1,423.36$; bootstrapped s.e.: 459.38; 95% CI = $-2,353.86$ to -575.25).

Specificity of the relationship between dFPN connectivity and build-up rate of evidence accumulation recapitulated in resting-state functional connectivity analyses. Our findings above highlight a specific relationship between macrostructural variation in the dorsal branch of the SLF, the build-up rate of evidence accumulation and the speed of perceptual reports. SLF1 is a large tract that connects several cortical areas, with many projections to dorsal frontoparietal regions. Thus, having identified a specific association between dorsal (but not ventral) SLF macrostructural organization and evidence accumulation build-up rate, we sought to confirm a critical role for the dFPN underpinning this observation. As such, we next asked whether this anatomical specificity would be recapitulated within a canonical, functionally defined dFPN brain network implicated in goal-directed stimulus processing, commonly referred to as the dorsal attention network^{47–50}. To this end, we investigated whether functional connectivity within this network, measured using multiband rs-fMRI, was related to the build-up rate of the CPP in a subset of 52 participants (27 female) aged between 18.89 and 36.92 years (mean age: 22.72 years; s.d. = 4.34 years). Using a previously published approach⁴⁶ (see Methods), two spherical seed regions were isolated to delineate both the dFPN and the functionally defined vFPN. The right-lateralized vFPN (or ventral attention network⁴⁸ receives projections from the ventral SLF branches⁴⁴, is densely connected with the locus coeruleus norepinephrine (noradrenergic) system⁵¹ and influences alertness and reorienting aspects of attention^{48,52,53}. The dFPN was defined using ROIs in the FEFs and IPS, whereas the vFPN was defined using seed ROIs in the temporoparietal junction (TPJ) and ventrofrontal cortex (VFC; see Methods). The whole-brain connectivity maps generated using this approach were consistent with previous work⁴⁷ (see Table 3, Fig. 3a and Extended Data Fig. 3).

To assess the relationship between evidence accumulation build-up rate and functional connectivity between the dFPN and the whole brain, CPP build-up rate was entered into a separate general linear model with the voxelwise functional connectivity maps of the dFPN. Age, gender and mean framewise displacement as a measure of in-scanner head motion were entered as nuisance covariates in the model (see also Supplementary Results 7 and Supplementary Fig. 9). With these confirmatory analyses, we hypothesised that increased dFPN functional connectivity would be associated with steeper CPP build-up rate. To investigate the specificity of the relationship between dFPN functional connectivity and evidence accumulation rate, this analysis was repeated with the vFPN. Finally, to test for specificity with respect to motor preparation signals and the FPN, the same analyses were repeated for LHB latency across the two networks.

The results for the dFPN showed that steeper CPP build-up rates were associated with stronger connectivity between the dFPN and the left premotor cortex (maximum $t_{47}=4.96$; $P=0.04$; $Z=4.62$; family-wise error-corrected cluster-level significance; cluster extent = 85 voxels; peak Montreal Neurological Institute (MNI) coordinates x , y and $z = -24$, -4 and 50 ; Fig. 3d), uncorrected for multiple EEG comparisons. There was no statistically significant relationship between LHB latency and connectivity differences

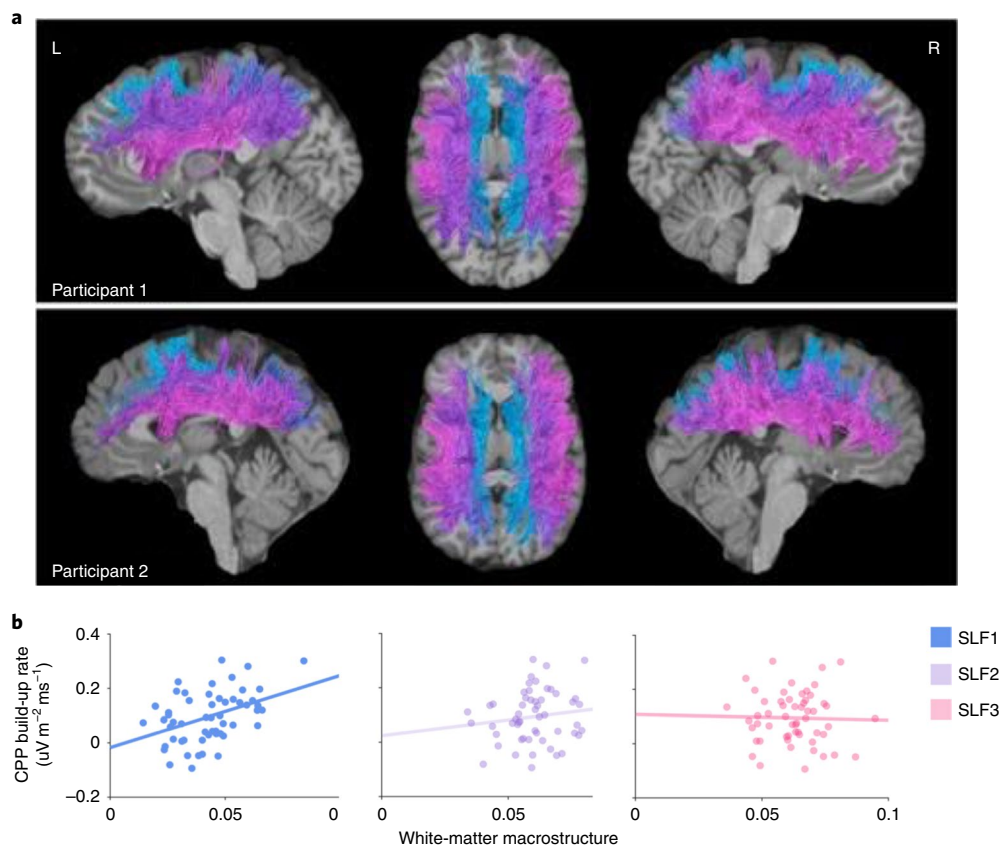


Fig. 2 | Relationship between evidence accumulation and white matter organization of the dorsal SLF. **a**, Delineation of the SLF in two example participants. L, left; R, right. **b**, CPP build-up rate is uniquely related to dorsal SLF volume ($n=56$; standardized $\beta=0.41$; $t=3.1$; $P=0.003$; 95% CI = 0.02 to 0.12; $BF_{10}=14.54$). Note that the x axes depict the tract volume divided by the whole-brain white matter mask. The direct relationships between the SLF tract measures and the EEG signals are plotted for visualization purposes only.

within the dFPN (maximum $t_{47}=4.4$; $P=0.82$). Furthermore, analyses for the vFPN revealed no statistically significant relationship between connectivity and either CPP build-up rate (maximum $t_{47}=4.2$; $P=0.99$) or LHB latency (maximum $t_{47}=5.02$; $P=0.31$).

To further test the specificity of our observed relationship between dFPN (but not vFPN) functional connectivity and CPP build-up rate, we delineated four additional networks (the salience, default mode, visual and basal ganglia networks) based on previously published seeds (respectively, refs. ^{10–13}; see Supplementary Table 3). To explore whether evidence accumulation rate was associated with functional connectivity between these networks and the whole brain, CPP build-up rate was regressed against the voxelwise functional connectivity maps for each of the respective maps. Again, age, gender and mean framewise displacement (as a measure of in-scanner head motion) were entered as nuisance covariates in these models, and to test for specificity with respect to motor preparation signals, the same analyses were repeated for LHB latency across the four networks. For these exploratory analyses, we applied Bonferroni correction for multiple comparisons to account for eight tests (two EEG metrics (CPP build-up rate and LHB latency) and four resting-state networks (Supplementary Table 3)).

The only result to pass the Bonferroni significance threshold was that steeper evidence accumulation rate was associated with stronger coupling between the visual network and a higher visual association region within the dFPN (Fig. 3 and Supplementary Results 5). This observation provides evidence for strong specificity: only one of the four additional networks showed a statistically significant association with behaviour and this association was between the visual network and a higher visual region that overlaps with both

the visual and dFPN (Fig. 3). We caution that although this analysis suggests that the correlations with evidence accumulation rate are specific to functional connectivity within the dFPN, we have not directly tested for a significant difference in the magnitude of the correlation observed across networks.

Together, these functional connectivity results recapitulate the structural connectivity findings and highlight a specific relationship between the dFPN and evidence accumulation (CPP) build-up rate.

Discussion

Here, we show that the network architecture of a discrete dorsal frontoparietal system critically influences the efficiency of perceptual decision-making. Specifically, our findings show that both structural and functional connectivity within the dFPN, but not the vFPN, vary according to an individual's rate of evidence accumulation and speed of perceptual decisions.

We observed that the white matter macrostructure (larger volume) of the most dorsal branch of the SLF (SLF1) is associated with a steeper evidence accumulation rate (build-up rate of the CPP). Within both hemispheres, SLF1 projects to regions comprising the dFPN, including the FEFs, IPS and dorsal premotor cortex^{39,44}. Neurophysiological recordings in animals have shown that decision variables build within each of these separate cortical areas^{13,15,16}, with each region governing slightly distinct aspects of the decision-making process^{8,54}. Although a multi-tiered neural architecture has been proposed to underlie perceptual decision-making^{54–57}, it has remained unclear how decision-relevant information is cohesively integrated across discrete cortical areas to influence action. Our findings highlight a distinct frontoparietal

Table 3 | Delineation of the dorsal and ventral attention networks

Seed	Contrast	Region(s)	Region (MNI2tal)	Peak MNI coordinates (x, y, z)	Maximum t value	Cluster extent (voxels)	P
Dorsal attention network							
FEF IPS	+		Right FEF peak; cluster extending to IPS	22, -16, 56	51.15	10,212	<0.0005
			Left IPS peak; cluster extending to FEFs	-26, -64, 58	13.73	4,024	<0.0005
			Right associative visual cortex	54, -60, -8	11.11	569	<0.0005
			Left associative visual cortex	-50, -68, -2	9.75	292	<0.0005
			Right IFG	54, 10, 28	9.04	151	<0.0005
Ventral attention network							
TPJ VFC	+		Right insula	40, 16, -4	37.28	3,112	<0.0005
			Right TPJ (angular gyrus)	54, -48, 18	27.37	3,682	<0.0005
			Right ACC	6, 22, 28	11.38	1,859	<0.0005
			Left insula	-40, 14, 2	10.90	982	<0.0005
			Right superior frontal gyrus	28, 50, 24	10.72	897	<0.0005
			Right precuneus	8, -46, 48	10.12	707	<0.0005
			Right lateral premotor cortex	48, 4, 50	9.91	245	<0.0005
			Left cerebellum	-22, -74, -32	9.60	208	<0.0005
			Left TPJ (angular gyrus)	-62, -50, 28	9.46	547	<0.0005

All P values are significant at a family-wise error rate of $P < 0.001$ and a cluster extent threshold of ten voxels. ACC, anterior cingulate cortex; IFG, inferior frontal gyrus.

white matter pathway that facilitates communication across these separate dFPN areas. Larger SLF1 volume may represent myriad physical characteristics of the tract, such as greater axonal diameter, higher packing density or thicker myelin^{58–61}. These attributes influence neurophysiological processes, such as conduction speed^{62,63}. As such, larger SLF1 volume probably enhances the efficacy of neural transmission within the dFPN with corresponding benefits for the timely coordination of activity across decision-relevant areas. Our results show that this relationship between stronger dFPN connectivity and faster perceptual reporting times is facilitated by steeper build rates of evidence accumulation. The observed effects cannot be attributed to generalized differences in frontoparietal white matter volume as evidence accumulation rate was not related to the macrostructural organization of the ventral projecting SLF branches (SLF2 and SLF3). Nor can these relationships be attributed to other neural signals that relate to the speed of perceptual reports, such as preparatory motor activity, since there was no association between SLF volume and LHB latency. These results therefore show a specific and unique association between individual differences in dorsal SLF1 volume and the speed of perceptual reports, which is mediated by the evidence accumulation process.

The dorsal SLF connects a prominent functional network (commonly referred to as the dorsal attention network^{48,52,53}). Our structural connectivity findings outlining a privileged relationship between the dFPN and sensory evidence accumulation were recapitulated in the confirmatory resting-state analyses such that connectivity within the dFPN varies as a function of evidence accumulation rate. More specifically, we observed that evidence accumulation rate is associated with increased coupling between the dFPN and left premotor cortex. Psychophysical and neurophysiological studies have indirectly shown that there is a continuous relay of information from regions underlying abstract evidence accumulation to areas governing motor execution^{4,64}. As such, greater connectivity between the dFPN and dorsal premotor cortex, which is densely connected with

the rest of the motor system^{65,66}, provides an efficient framework for communicating graded levels of the perceptual decision to the motor system^{67,68} (see also Supplementary Discussion). Evidence accumulation build-up rate was additionally related to increased functional coupling between the visual network and a higher visual association that overlaps with the dFPN. This accords with animal neurophysiology work^{69,70} and suggests that activity in early visual areas may actively accumulate sensory evidence—a phenomenon probably influenced by top-down modulatory input from the dFPN^{71,72}.

Previous work has shown the CPP to be analogous to the P300, or centro-parietal P3(b) component¹⁴. Both signals have centro-parietal positive polarity, are elicited by goal-relevant stimuli, demonstrate insensitivity to stimulus modality and covary with perceptual performance. Twomey et al.⁷³ made a key advance in establishing the functional equivalence of these signals by analysing the P300 in the context of the oddball task, which is often used to elicit the P300. Twomey and colleagues demonstrated that the P300 exhibited the key characteristics of an evidence accumulation signal: its build-up rate scaled with evidence strength; it accounted for independent variance in reaction time; and its amplitude reached a stereotypical threshold before a participants' report. In fact, although early research suggested a role for the P300 in decision-making (for example, refs. ^{74,75}), this proposed association was never linked to a specific computational process. Subsequent competing explanatory accounts implicated the P3b in a diversity of other cognitive processes^{76–78} and a consensus regarding its precise role was never reached. The study by Twomey et al. was, to our knowledge, the first to place the P300 with a well-defined computational framework. Reconceptualizing the P300 within a decision-making framework facilitates the interpretation of its modulation by a range of experimental conditions and brain disorders^{76–80}.

In accordance with our findings that a discrete dFPN system underpins evidence accumulation build-up rate, functional neuroimaging and intracranial EEG investigations have localized the

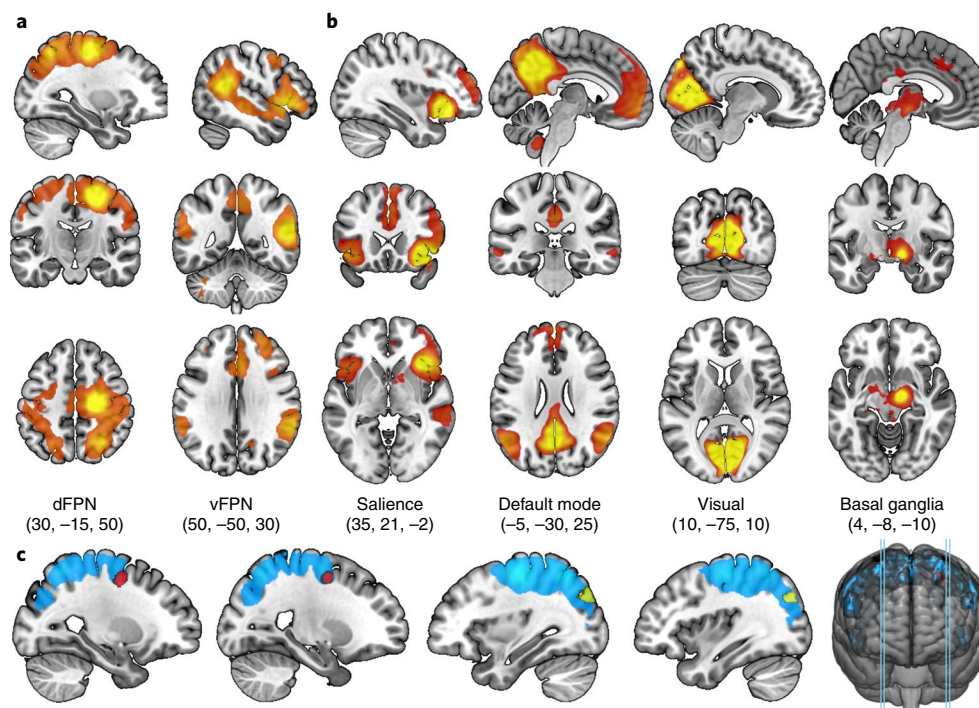


Fig. 3 | Relationship between dFPN connectivity and build-up rate of evidence accumulation recapitulated with rs-fMRI functional connectivity.

a. The dFPN (delineated using FEF and IPS seeds) and vFPN (delineated using TPJ and VFC seeds) in a subset of $n=52$ participants during rs-fMRI. **b.** Salience, default mode, visual and basal ganglia networks (delineated using V1, orbito fronto-insular, posterior cingulate and subthalamic nucleus seeds, respectively) in $n=52$ participants during rs-fMRI. Note that for both **a** and **b**, areas most strongly correlated with the seed regions are in yellow, and areas least strongly correlated with the seed regions are in red. The numbers in parentheses denote the MNI coordinates (x, y, z) of the displayed slices. **c.** The dFPN is depicted in blue (thresholded using a family-wise error (FWE) rate of $P < 0.001$ and an extent threshold of ten voxels). CPP build-up rate was associated with increased coupling between the dFPN and the left dorsal premotor cortex (red; maximum $t_{47}=4.96$; $P=0.04$; $Z=4.62$; FWE-corrected cluster-level significance; cluster extent = 85 voxels; peak MNI coordinates x, y and $z = -24, -4$ and 50). CPP build-up rate was additionally associated with increased coupling between the visual network and a higher visual area (yellow; maximum $t_{47}=5.46$; $P=0.003$; $Z=4.78$; FWE-corrected cluster-level significance; cluster extent = 127 voxels; peak MNI coordinates x, y and $z = 30, -84$ and 38), which overlapped with both the visual network and the dFPN. The blue vertical lines in the right-most image highlight the slices selected to display the preceding images. Note that, for the purpose of visualization, the statistical maps display significant FWE-corrected clusters ($P < 0.05$) and thresholded t values for visualization purposes at $P < 0.001$.

P300 in humans, at least in part, to dFPN structures^{37,38}. Clinically relevant differences in the P300 have been noted in several neurological and psychiatric populations, including ADHD, schizophrenia and Alzheimer's disease^{81–83}. Of note, these clinical disorders are often characterized by both structural and functional abnormalities in dFPN regions^{25,26}. Longitudinal interventions (such as meditation) that induce white matter plasticity in the SLF^{40,41} have recently been shown to alter P3b dynamics⁸⁴. Similarly, methylphenidate (a gold-standard pharmacological treatment for ADHD⁸⁵ that modulates activity in brain regions including the dFPN) increases evidence accumulation (CPP) build-up rate⁸⁶. As such, the results of the present study, as well as past findings, have significant translational potential. Specifically, we highlight a structural and functional network that could be strengthened using a range of neurorehabilitation techniques (for example, brain stimulation, pharmacological and behavioural interventions and fMRI neurofeedback). Moreover, we outline a neurophysiological marker of evidence accumulation that could be used as a surrogate biomarker for tracking the efficiency of interventions aimed at enhancing decision-making processes in clinical groups.

Our results outline a specific network architecture relating to the efficiency of human perceptual decision-making. We have highlighted a structural and functional architecture that coordinates the communication of decision-relevant information throughout the dFPN in humans. Specifically, our findings show that stronger connectivity between the FEF, IPS and premotor cortex is associated

with faster evidence accumulation and a more efficient transformation of incoming sensory information into action. A limitation of the present study is the capacity to infer causality about the direction of this relationship. An interesting avenue for future longitudinal work will be to disentangle to what extent pre-existing structural conditions within SLF1 determine individual differences in the CPP build-up rate (for example, through genetic influences^{39,87}) or whether the efficiency of everyday evidence accumulation induces experience-dependent white matter plasticity in the FPN. The findings provide a network architecture supporting the evidence accumulation process in humans.

Methods

Experimental model and participant details. *Participants.* The experimental protocol was approved by Monash University's Human Research Ethics Committee before testing and was carried out in accordance with the approved guidelines. Informed consent was obtained from all participants before testing. Participants were paid AU\$30 for participating in the EEG session and AU\$50–100 for participating in the genetics of cognition project, which involved neuroimaging, as well as (neuro)psychological and cognitive assessments. Fifty-six healthy right-handed participants (29 female) aged between 18.03 and 36.92 years (mean age: 22.66 years (s.d.: 4.23 years) reporting normal or corrected-to-normal vision, no history of neurological or psychiatric disorder and no head injury resulting in loss of consciousness were recruited for the study. The participants were a subset of individuals who had previously participated in an EEG study at Monash University, Melbourne, Australia⁸⁸ and had also undergone neuroimaging, including a resting-state scan and white matter diffusion imaging. This study did not involve the randomization of participants to conditions, and data collection and analysis

were not performed blind to the conditions of the experiments. All statistical tests were two tailed and used an alpha level of 0.05. Please note that our sample of $n = 56$ participants is larger than comparable studies published previously^{44,89,90}. To calculate post-hoc power analyses, we used an effect size of Cohen's $f = 0.56$. We determined this value based on the relationship between lateralization of SLF1 organization and lateralization of gamma modulation reported in ref.⁸⁹ ($r^2 = 0.36$; Cohen's $f = (1/(1 - 0.36)) = 0.56$). Our analyses indicated that $n = 56$ participants facilitates the detection of a large effect (0.56) of the relationship between the white matter structure of SLF1 and the neurophysiological signatures of interest (CPP build-up rate and LHB latency; $\alpha = 0.05$) with 99% power.

Methods details. Neurophysiological investigation of the speed of perceptual reports. EEG recordings were taken continuously while participants performed a variant of the random-dot motion perceptual decision-making task (Fig. 1)^{1,25,42}. As previously described in ref.⁸⁸, during this task, participants fixated centrally and monitored two patches of 150 moving dots that were presented peripherally in each hemifield. The dot stimuli flickered on and off the screen every 23.5 ms, resulting in a flicker rate of 21.25 frames per second (each frame representing two screen refreshes). During random motion, these dots were placed randomly throughout the patch on each frame. During coherent motion, within one hemifield, a proportion (50%) of the dots were randomly selected on each frame to be displaced in a downward direction on the following frame, with a motion speed of 6° per second. Targets were defined by this seamless transition from random motion to coherent motion in a downward direction (Fig. 1; note that the images in Figs. 1–3 are composite images). Participants signalled target identification with a speeded button press using their right index finger (response time). Accuracy was at ceiling during the task (mean: 98%; s.d.: 2.6; range: 91–100%). Targets were separated by intervals of random motion of 3.06, 5.17 or 7.29 s (randomized throughout each block). Participants completed 16 blocks consisting of 18 targets, with each block lasting 3 min. Participants were given a break of 30 s between each block. An SR Research EyeLink eye tracker (EyeLink version 2.04; SR Research/SMI) recorded eye movements to ensure that participants maintained fixation. The centre of each random-dot motion patch was at a visual angle of 10° either side and 4° below the fixation square; each patch covered a visual angle of 8° and consisted of 150 6 pixel × 6 pixel white dots. The model was run using MATLAB (MathWorks) and the Psychophysics Toolbox extensions^{91–93}.

EEG pre-processing. As described by Newman et al.⁸⁸, continuous EEG recordings were acquired from 64 scalp electrodes using a BrainAmp DC system (Brain Products) digitized at 500 Hz. Data were processed using a combination of custom scripts and EEGLAB⁹⁴ routines implemented in MATLAB (MathWorks), and event-related potential (ERP) waves were visualized using GRAMM⁹⁵ (MATLAB). A 35-Hz low-pass filter was applied to the data off-line using a fourth-order Butterworth filter. Noisy channels were interpolated via spherical spline and the data were re-referenced to the average reference. Epochs were extracted from the continuous data from −700 to 1,800 ms around target onset. For the ERP signals, the epochs were base-lined with respect to 100 to 0 ms before target onset. The baseline window for the spectral measures (pre-target alpha and LHB) was −500 to −400 ms. A trial was excluded from the analysis if any of the following conditions applied: (1) response times were ≤ 150 ms (pre-emptive responses) or $\geq 1,800$ ms (responses after coherent motion offset); (2) the EEG from any channel exceeded 100 V during the interval from 100 ms before target onset to 100 ms after response time; or (3) central fixation was broken by blinking or eye movement 3° left or right of the centre during the interval between 100 ms before target onset and 100 ms after response. To minimize the interaction between overlapping ERP components, the data were subjected to current source density transformation⁹⁶.

The N2c and N2i components were measured contra- and ipsilateral to the target location, respectively, at electrodes P7 and P8 (refs.^{25,88}). The CPP was measured at electrode Pz^{4,20,25,73,88} and the FCN⁴ was measured at peak electrode FCz.

The N2c, CPP and FCN signals were aggregated to average waveforms as a function of target hemifield for each participant. N2c latency was identified as the time point with the most negative amplitude value in the stimulus-locked waveform between 150 and 400 ms, while N2c amplitude was measured as the mean amplitude inside a 100-ms window centred on the stimulus-locked grand average peak of the N2c (256 ms) collapsed across hemifield²⁵. Onset latency of the CPP was measured by performing running sample point by sample point t -tests against zero using a 25-ms sliding window across each participant's stimulus-locked CPP waveforms. CPP onset was defined as the first point at which the amplitude reached significance at the 0.05 level for 15 consecutive points^{25,97,98}. CPP build-up rate was defined as the slope of a straight line fitted to the response-locked waveform^{4,20}, with the time window defined individually for each participant as 100 ms pre-response. CPP and FCN amplitudes were measured as the mean amplitude within the same 100-ms pre-response window.

Pre-target alpha and LHB power were calculated using the temporal spectral evolution approach³⁹. All epochs were bandpass filtered (alpha: 8–14 Hz; beta: 20–35 Hz), converted to absolute values (rectified) and trimmed by 200 ms at each end of the epoch to remove filter warm-up artefacts. The data were then smoothed by averaging within a 100-ms moving window, moving incrementally forward

in 50-ms increments. Alpha was measured bilaterally at peak occipito-parietal electrode locations PO3/PO7 (left hemisphere) and PO4/PO8 (right hemisphere) as the mean power from 400 to 0 ms before the onset of the target. LHB latency was measured within the left hemisphere motor site (C3) as the most negative-going point between 0 and 850 ms. To verify the validity of LHB latency as a marker of motor preparatory activity, several additional analyses were conducted (Supplementary Results 6 and Supplementary Fig. 3).

Diffusion MRI acquisition. Neuroimaging data were acquired on a Siemens MAGNETOM Skyra 3 T MRI scanner (Erlangen, Germany). T1-weighted anatomical images were acquired using magnetization-prepared rapid gradient-echo imaging (repetition time = 2,300 ms; echo time = 2.07 ms; flip angle: 9°; voxel size = 1.0 mm³). High-angular diffusion-weighted imaging data were acquired using a b value of 3,000 s mm^{−2} along 60 directions (repetition time = 8,800 ms; echo time = 110 ms; echo spacing = 0.61 ms; field of view (FOV) = 240 mm; flip angle: 90°; 2.5 mm isotropic). Additionally, seven images with no diffusion weighting ($b = 0$) were collected. The diffusion-weighted imaging series was acquired using a right–left phase encoding direction, and reverse phase encoding data were also acquired (left–right) for susceptibility distortion correction.

Diffusion MRI pre-processing and tractography. Diffusion data were pre-processed using the MRtrix3 (version 0.3.15; <https://github.com/MRtrix3>) software package, which included denoising, motion, eddy current and susceptibility distortion correction¹⁰⁰, as well as bias field correction. A response function was estimated for each participant, followed by the generation of a fibre orientation distribution map for each participant. In addition, tensor-derived fractional anisotropy scalar maps were generated. T1 images were registered to diffusion space using a linear registration¹⁰¹. Subsequently, anatomically constrained tractography was performed¹⁰² to constrain whole-brain tractography to the white matter/grey matter boundary. Constrained tractograms were generated using 2 million streamlines, seeding from the white/grey interface. Head motion occurring during diffusion acquisition was quantified by deriving framewise displacement as per previously published work^{103–105}. Mean framewise displacement was calculated as the mean displacement between diffusion volumes using the `fsl_motion_outliers` FSL toolbox (version 6.0).

Dissection of the SLF. Virtual dissection of the three segments of the SLF (SLF1, SLF2 and SLF3; see Fig. 2) in each hemisphere was carried out using a multiple ROI approach previously described⁴⁴. First, to generate standardized ROIs across individuals and avoid any experimenter-biases in individual SLF estimates, a cohort-specific T1 template was created by collating all 56 T1-weighted anatomical scans using the Advanced Normalisation Tools (ANTs; <http://stnava.github.io/ANTs/>). We then used this template brain to generate ROIs using the previously validated approach^{44,89,90}. Specifically, include and exclude ROIs were manually drawn on the template brain in relation to anatomical landmarks described below⁴⁴ (Extended Data Fig. 4). To ensure standardised ROIs across participants, the ROIs were then reverse transformed into each participant's individual native space using an inverted nonlinear symmetric and diffeomorphic warp.

The primary include ROIs were defined using coronal slices corresponding to the level of the anterior commissure (AC) and posterior commissure (PC; see Extended Data Fig. 4). At the level of the AC, three ROIs were drawn to delineate the superior, middle and inferior frontal gyri. At the level of the PC, a single large parietal ROI was drawn. A number of exclude ROIs were also used in order to optimize the characterization of each tract. To exclude streamlines of the arcuate fasciculus, an exclude ROI was drawn on the axial slice, the level of the base of the splenium of the corpus callosum. The ROI was drawn from the most lateral portion of the ventricle horn and covered the temporal lobe. Other large ROIs were used to exclude extraneous streamlines travelling across the midline slice, down the brainstem or along the internal and external capsule. For dissecting the most dorsal branch (SLF1), streamlines had to pass through both the superior frontal and parietal ROIs, for the second branch (SLF2), streamlines had to pass through both the middle frontal and parietal ROIs, and for the most ventral branch (SLF3), streamline had to pass through both the inferior frontal and parietal ROIs. For each tract the exclusion ROIs were: (1) the other two corresponding ROIs at the level of the AC; (2) the arcuate fasciculus ROI; (3) midline; (4) brainstem; and (5) internal and external capsule. Whole-brain tractography was filtered using the include and exclude ROIs in native space, then converted to a probability map of the number of streamlines passing through each voxel.

The generated fibre pathways were visually inspected for anatomical correctness. Images were binarized to calculate the tract volume (macrostructure) and mean FA (microstructure). Please see Fig. 2 for examples of the SLF dissection in two individuals. In order to control for individual differences in overall white matter volumes, SLF volume estimations were divided by the whole-brain white matter mask for each tract in question (for example, reported SLF1 volumes refer to % SLF1 volume/whole-brain white matter mask). To validate previous reports of a bilaterally organised dorsal SLF (SLF1) and a right-lateralized ventral branch (SLF2^{44,89}, hemispheric differences in tract volume were explored using paired sample t -tests, Bonferroni corrected for multiple comparisons ($\alpha/3$). Results

revealed no statistically significant hemispheric differences in tract volume for the SLF1 ($t_{55} = -2.02$; $P = 0.05$) or SLF2 ($t_{55} = 1.8$; $P = 0.08$). Right-lateralization was observed for the SLF3 ($t_{55} = -9.5$; $P < .0005$), with a larger branch in the right ($M = 0.07\%$; $s.d. = 0.014$) relative to left ($M = 0.05\%$; $s.d. = 0.013$) hemisphere (Extended Data Fig. 5).

rs-fMRI acquisition. Eyes closed resting-state multiband T2*-weighted whole-brain echo-planar images (EPIs) were acquired for each participant using a 3 T Siemens Skyra MRI scanner, equipped with a 32-channel head coil, located at the Monash Biomedical Imaging facility, Melbourne, Australia. For each participant, 620 functional volumes with 42 slices each were acquired using an interleaved acquisition with the following parameters: repetition time of 754 ms, echo time of 21 ms, flip angle of 50°, multiband acceleration factor of 3, FOV of 190 mm, slice thickness of 3 mm, and 3 mm isotropic voxels. We also acquired anatomical T1-weighted images for each participant using a three-dimensional magnetic-prepared rapid gradient-echo sequence. For each participant, 192 slices were acquired using an ascending acquisition with the following parameters: repetition time of 2,300 ms, echo time of 2.07 milliseconds, flip angle of 9°, FOV of 256 mm, and 1-mm isotropic voxels.

rs-fMRI pre-processing. Following acquisition, scans were checked for artefacts using MRIQC, an automated pipeline for quality checking of MRI scans¹⁰⁶, as part of a larger imaging study ($n = 441$ participants). Based on the reports, poor quality scans were removed from subsequent analyses. Initial pre-processing of EPI images was carried out using FSL FEAT, with the following procedure: removal of the first four volumes, rigid-body head motion correction, 3 mm spatial smoothing to improve signal-to-noise ratio, and high-pass temporal filter of 75 s. Following basic pre-processing, spatial independent component analysis (ICA) was performed on the EPI data using FSL MELODIC. The independent components were used as input into FSL-FIX, an ICA based denoising approach that utilizes an automated classifier to identify noise components and subsequently remove them from the data^{107,108}. The approach has been shown to efficiently remove motion and physiological noise, along with artefacts associated with multiband acceleration acquisition^{107,109}. We used a classifier that was trained on data from an independent sample of 25 individuals with the same scanner and acquisition parameters. Based on spatial characteristics, time-series fluctuations, and power spectra, we hand-trained the classifier by manually labelling over 2,000 components as signal or noise¹¹⁰.

Subsequently, the mean global signal from the entire brain was regressed from the data by taking the averaged signal from a whole-brain mask. We also removed the first derivative and squared signal and first derivative of the squared signal¹¹¹. This step has been shown to result in an optimal motion artefact removal following FSL-FIX¹¹². Head motion is a known problem in fMRI^{111,113}, which we addressed here using a combination of ICA-FIX¹¹⁰ and global signal regression (GSR). Consistent with past work^{111,112,114}, these procedures successfully removed any correlations between functional connectivity and head motion (see Supplementary Methods for details). Although GSR is a controversial procedure^{115,116}, it is the only readily-usable technique that can reduce widespread respiratory- and motion-related fluctuations in the fMRI signal, which have a major impact on functional connectivity estimates¹¹⁴. The degree to which these procedures may be too conservative and remove neural signal is unclear, although recent evidence indicates that GSR actually enhances brain-behaviour associations¹¹⁷.

Functional data were then spatially normalized to the MNI space using ANTs (version 2.2.0). Normalization was performed in a three-step method: (1) registration of the mean realigned functional scan to the skull-stripped anatomical T1 scan via a linear registration; (2) spatial normalization of the anatomical scan to the MNI template via a nonlinear registration; and (3) normalization of the functional scan to the MNI template using a transform from step 1 and 2 concatenated in a single transformation matrix. The final pre-processing step involved spatial smoothing of normalized data with a 6 mm full-width half-maximum Gaussian kernel, performed using the 3dBlurToFWHM function in AFNI (version 16).

To control for movement artefacts during scanning, mean framewise displacement was used as an index of in-scanner head movement¹⁰³. Mean framewise displacement (mFD) for each participant was estimated using the root mean squared volume-to-volume displacement of all voxels, derived from six head motion parameter estimates (three translations, three rotations; Jenkinson, Bannister, Brady and Smith, 2002). Participants were excluded from analysis if their mFD exceeded 0.11 mm. This threshold was determined by concatenating all participants' mFD values (from a larger imaging sample of 441 participants) into a single distribution and setting a threshold at the 75th percentile plus 1.5 times the interquartile range. This approach is similar to the `fsl_motion_outliers` function of the FSL toolbox. Based on this value, participants were removed from further analysis using the following criteria: (1) their mean framewise displacement was greater than 0.11 mm; (2) the sum of suprathreshold spikes was greater than 20%; or (3) any framewise displacement was greater than 2.5 mm (this value was adapted from previous work¹¹⁸). This procedure resulted in the exclusion of 32 individuals from the larger sample.

Delineation of the functional connectivity networks using rs-fMRI. First, to verify that the observed relationship between SLF1 dFPN white matter organization and CPP build-up rate would be recapitulated in dFPN functional connectivity, the dorsal and ventral attention networks were delineated using a seed-based analysis used in previously published work⁴⁷. Four ROIs (two dorsal and two ventral) were selected as a priori spherical seed ROIs (12 mm³ radius), which were previously shown to correlate with resting-state fluctuations in networks resembling the dorsal and ventral attention network⁴⁷. The dorsal attention network ROIs included the right IPS and the right FEF. ROIs corresponding to the ventral attention network were seeded in the right TPJ and the right VFC (for seed coordinates, see Supplementary Table 3).

First- and second-level analyses were performed using SPM8. To model the blood oxygen level-dependent signal fluctuations in each voxel, for each participant, time courses of each ROI were entered as a covariate into a general linear model. This step yielded one whole-brain functional connectivity map for each ROI, leading to a total of four maps per participant that corresponded to the IPF, FEF, TPJ and VFC seeds.

To define the dorsal attention network, whole-brain voxelwise functional connectivity with the right IPS and the right FEF seeds was estimated. This was done by entering each participant's whole-brain functional connectivity maps of the right IPS and right FEF seeds from the first-level analysis into a second-level general linear model to generate a group-wide map of common regions that are functionally connected to the right IPS and FEF, thus comprising the dorsal attention network. The ventral attention network was delineated using a similar method by identifying common brain regions that are functionally connected to the TPJ and VFC seeds in a group-wide, second-level general linear model. Refer to Table 3 for regions that are functionally connected to the FEF and IPS and TPJ and VFC.

Second, to further test the specificity of the association between dFPN connectivity and evidence accumulation rate, we delineated four additional networks (the salience, default mode and visual and basal ganglia networks) based in the fronto-insular, posterior cingulate/precuneus, primary visual cortex (V1) and subthalamic nucleus seed regions, respectively (Supplementary Table 3 and Fig. 3b)^{119–122}.

To assess the relationship between EEG markers of perceptual decision-making and functional connectivity of the resting-state networks with the rest of the brain, the EEG signals of interest (CPP build-up rate and LHB latency) were entered into a general linear model with voxelwise functional connectivity maps of the relevant networks. Each covariate of interest was modelled separately against each of the networks. Nuisance covariates were entered into all models and included age, sex and mean framewise displacement as a measure of in-scanner head motion. Further motion checks are additionally reported in Supplementary Results 7 and Supplementary Fig. 4.

Statistical analysis. Data distribution was assumed to be normal for the following variables (Supplementary Fig. 5), but this was not formally tested.

Relationship between behaviour and EEG. To assess whether inter-individual differences in response time during perceptual decision-making varied as a function of EEG signals of perceptual decision-making, the EEG parameters were each added sequentially into regression models in a hierarchical fashion⁴⁸. The order of entry was determined by the temporal order in the perceptual decision-making process: pre-target attention levels (alpha power); early target selection (N2c amplitude and latency); evidence accumulation (CPP onset, build-up rate and amplitude); frontal preparatory activity (FCN amplitude); and motor preparation (left lateralized beta latency). This hierarchical entry method was implemented to assess whether each of the separate neurophysiological signals improved the model fit for response time over and above the signals that temporally preceded them. All neurophysiological signals that improved the model fit for response time were entered into a separate regression model to obtain accurate parameter estimates. Age and gender (covariates of disinterest) were entered together as the first predictor in the model. Note that all statistical tests were two sided and effect sizes of regression models were calculated using Cohen's f using the following formula: $(R^2/(1 - R^2))$.

Relationship between SLF organization and neurophysiology. To model inter-individual differences in macro- and microstructural organization of the dorsal SLF as a function of neurophysiological signals predicting perceptual decision-making performance, CPP build-up rate and LHB latency were entered into separate regression models for both volume and fractional anisotropy. To confirm the specificity of the results to the dorsal tract, these regression models were also explored for the other two SLF branches. The individual β values from these analyses were Bonferroni corrected for multiple comparisons ($\alpha/12$).

Confirmatory statistics using Bayes factor analyses. A disadvantage of null hypothesis significant testing is that non-significant P values cannot be interpreted as support for the null hypothesis⁴³. To circumvent this issue and confirm whether the non-significant findings reported for the relationships between behaviour, neurophysiology and SLF organization represent support for the null hypothesis,

we ran Bayes factor analyses in JASP (version 0.11.1). We calculated the Bayes factor inclusion probabilities (BF_{10}) using a Jeffrey–Zellner–Siow prior¹²³ (using the default settings in JASP, r scale covariates = 0.354). A Jeffrey–Zellner–Siow Bayes factor BF_{01} can be interpreted such that a value of 3 indicates three times more support for the null hypothesis than the alternative hypothesis and a value of one-third indicates three times more support for the alternative than the null hypothesis. We report BF_{10} values, whereby values above 1 indicate strength of evidence in favour of the alternative hypothesis and values below 1 indicate strength of evidence in favour of the null hypothesis.

Mediating effect of neurophysiology on the relationship between SLF organization and performance. To elucidate the mediating effect of evidence accumulation rate on the relationship between inter-individual differences in SLF organization and perceptual decision-making performance, bootstrapped mediation analyses (5,000 samples) were performed using the PROCESS computational toolbox^{45,46}. The plausibility of a causal model was assessed whereby the dorsal SLF tract (predictor variable X) causally influences the evidence accumulation rate (CPP build-up rate; mediator variable(s) M), which in turn exerts a causal influence on behavioural performance (response time; outcome variable Y). The CIs reported for the indirect effect in the main text are bootstrapped CIs based on 5,000 samples. Mediation analyses are considered significant when the bootstrapped CI does not contain zero.

It is noteworthy that mediation analyses have historically been conducted on the condition that X is directly associated with Y (that is, a direct effect; for example, ref. ¹²⁴). However, there is growing consensus that a direct relationship between X and Y is not a prerequisite for exploring mediation effects (that is, lack of correlation between X and Y does not discount a mediating effect of M). Rather, current mediation analyses explore whether X exerts a causal influence on M , which in turn causally influences Y ⁹⁶.

Reporting Summary. Further information on research design is available in the Nature Research Reporting Summary linked to this article.

Data availability

The EEG dataset from the current study is available at the following repository: <https://figshare.com/s/8d6f461834c7180a444>. These data are open access and available under a Creative Commons attribution: NonCommercial-ShareAlike 3.0 international licence. Raw data for the diffusion and resting-state imaging were collected at the Turner Institute for Brain and Mental Health as part of a large-scale project. Derived diffusion and resting-state MRI data supporting the findings of this study are available from the corresponding author upon request.

Code availability

All EEG pre-processing scripts implemented in this study are available from https://github.com/gerontium/big_dots. These scripts are open access and available under a Creative Commons attribution: NonCommercial-ShareAlike international license. Custom code for the resting-state MRI and EEG data that the support the conclusion of this article are available from the corresponding author upon request.

Received: 12 February 2019; Accepted: 16 March 2020;

Published online: 20 April 2020

References

1. Fish, S. et al. Modelling reaction time distribution of fast decision tasks in schizophrenia: evidence for novel candidate endophenotypes. *Psychiatry Res.* **269**, 212–220 (2018).
2. Fosco, W. D., White, C. N. & Hawk, L. W. Acute stimulant treatment and reinforcement increase the speed of information accumulation in children with ADHD. *J. Abnorm. Child Psychol.* **45**, 911–920 (2016).
3. Huang, Y.-T. et al. Different effects of dopaminergic medication on perceptual decision-making in Parkinson's disease as a function of task difficulty and speed–accuracy instructions. *Neuropsychologia* **75**, 577–587 (2015).
4. Kelly, S. P. & O'Connell, R. G. Internal and external influences on the rate of sensory evidence accumulation in the human brain. *J. Neurosci.* **33**, 19434–19441 (2013).
5. Twomey, D. M., Kelly, S. P. & O'Connell, R. G. Abstract and effector-selective decision signals exhibit qualitatively distinct dynamics before delayed perceptual reports. *J. Neurosci.* **36**, 7346–7352 (2016).
6. White, C. N., Ratcliff, R., Vasey, M. W. & McKoon, G. Using diffusion models to understand clinical disorders. *J. Math. Psychol.* **54**, 39–52 (2010).
7. Starns, J. J. The effects of aging on the speed–accuracy compromise: boundary optimality in the diffusion model. *Psychol. Aging* **2**, 277–390 (2010).
8. Hanks, T. D. & Summerfield, C. Perceptual decision making in rodents, monkeys, and humans. *Neuron* **93**, 15–31 (2017).
9. Roitman, J. D. & Shadlen, M. N. Response of neurons in the lateral intraparietal area during a combined visual discrimination reaction time task. *J. Neurosci.* **22**, 9475–9489 (2002).
10. Shadlen, M. N. & Shohamy, D. Decision making and sequential sampling from memory. *Neuron* **90**, 927–939 (2016).
11. Ding, L. & Gold, J. I. Caudate encodes multiple computations for perceptual decisions. *J. Neurosci.* **30**, 15747–15759 (2010).
12. Ratcliff, R., Chierian, A. & Segraves, M. A comparison of macaque behavior and superior colliculus neuronal activity to predictions from models of two-choice decisions. *J. Neurophysiol.* **90**, 1392–1407 (2003).
13. Cisek, P. & Kalaska, J. F. Neural correlates of reaching decisions in dorsal premotor cortex: specification of multiple direction choices and final selection of action. *Neuron* **45**, 801–814 (2005).
14. Pape, A.-A. & Siegel, M. Motor cortex activity predicts response alternation during sensorimotor decisions. *Nat. Commun.* **7**, 13098 (2016).
15. Ding, L. & Gold, J. I. Neural correlates of perceptual decision making before, during, and after decision commitment in monkey frontal eye field. *Cereb. Cortex* **22**, 1052–1067 (2012).
16. Huk, A. C. Neural activity in macaque parietal cortex reflects temporal integration of visual motion signals during perceptual decision making. *J. Neurosci.* **25**, 10420–10436 (2005).
17. Hanks, T., Kiani, R. & Shadlen, M. N. A neural mechanism of speed–accuracy tradeoff in macaque area LIP. *eLife* **3**, e02260 (2014).
18. Heitz, R. P. & Schall, J. D. Neural mechanisms of speed–accuracy tradeoff. *Neuron* **76**, 616–628 (2012).
19. Thura, D. & Cisek, P. Modulation of premotor and primary motor cortical activity during volitional adjustments of speed–accuracy trade-offs. *J. Neurosci.* **36**, 938–956 (2016).
20. O'Connell, R. G., Dockree, P. M. & Kelly, S. P. A supramodal accumulation-to-bound signal that determines perceptual decisions in humans. *Nat. Neurosci.* **15**, 1729–1735 (2012).
21. De Lange, F. P., Rahnev, D. A., Donner, T. H. & Lau, H. Prestimulus oscillatory activity over motor cortex reflects perceptual expectations. *J. Neurosci.* **33**, 1400–1410 (2013).
22. Steinemann, N. A., O'Connell, R. G. & Kelly, S. P. Decisions are expedited through multiple neural adjustments spanning the sensorimotor hierarchy. *Nat. Commun.* **9**, 3627 (2018).
23. De Lange, F. P., Jensen, O. & Dehaene, S. Accumulation of evidence during sequential decision making: the importance of top–down factors. *J. Neurosci.* **30**, 731–738 (2010).
24. Donner, T. H., Siegel, M., Fries, P. & Engel, A. K. Buildup of choice-predictive activity in human motor cortex during perceptual decision making. *Curr. Biol.* **19**, 1581–1585 (2009).
25. Loughnane, G. M. et al. Target selection signals influence perceptual decisions by modulating the onset and rate of evidence accumulation. *Curr. Biol.* **26**, 496–502 (2016).
26. Wyart, V., de Gardelle, V., Scholl, J. & Summerfield, C. Rhythmic fluctuations in evidence accumulation during decision making in the human brain. *Neuron* **76**, 847–858 (2012).
27. Murphy, P. R., Robertson, I. H., Harty, S. & O'Connell, R. G. Neural evidence accumulation persists after choice to inform metacognitive judgments. *eLife* **4**, e11946 (2015).
28. Philiastides, M. G., Heekeren, H. R. & Sajda, P. Human scalp potentials reflect a mixture of decision-related signals during perceptual choices. *J. Neurosci.* **34**, 16877–16889 (2014).
29. Rungtameeetaweemana, N., Ithipuripat, S., Salazar, A. & Serences, J. T. Expectations do not alter early sensory processing during perceptual decision-making. *J. Neurosci.* **38**, 5632–5648 (2018).
30. Spitzer, B., Waschke, L. & Summerfield, C. Selective overweighting of larger magnitudes during noisy numerical comparison. *Nature* **1**, 0145 (2017).
31. Von Lautz, A., Herding, J. & Blankenburg, F. Neuronal signatures of a random-dot motion comparison task. *NeuroImage* **193**, 57–66 (2019).
32. Van Vugt, M. K., Beulen, M. A. & Taatgen, N. A. Relation between centro-parietal positivity and diffusion model parameters in both perceptual and memory-based decision making. *Brain Res.* **1715**, 1–12 (2019).
33. Afacan-Seref, K., Steinemann, N. A., Blangero, A. & Kelly, S. P. Dynamic interplay of value and sensory information in high-speed decision making. *Curr. Biol.* **28**, 795–802.e6 (2018).
34. Herding, J., Ludwig, S., von Lautz, A., Spitzer, B. & Blankenburg, F. Centro-parietal EEG potentials index subjective evidence and confidence during perceptual decision making. *NeuroImage* **201**, 116011 (2019).
35. Tagliabue, C. F. et al. The EEG signature of sensory evidence accumulation during decision formation closely tracks subjective perceptual experience. *Sci. Rep.* **9**, 4949 (2019).
36. Jurkiewicz, M. T., Gaetz, W. C., Bostan, A. C. & Cheyne, D. Post-movement beta rebound is generated in motor cortex: evidence from neuromagnetic recordings. *NeuroImage* **32**, 1281–1289 (2006).
37. Soltani, M. & Knight, R. T. Neural origins of the P300. *Crit. Rev. Neurobiol.* **14**, 199–224 (2000).

38. Linden, D. E. J. The P300: where in the brain is it produced and what does it tell us? *Neuroscientist* **11**, 563–576 (2005).
39. Stuss, D. T. & Knight, R. T. *Principles of Frontal Lobe Function* (Oxford Univ. Press, 2002).
40. Tang, Y.-Y. et al. Short-term meditation induces white matter changes in the anterior cingulate. *Proc. Natl Acad. Sci. USA* **107**, 15649–15652 (2010).
41. Tang, Y.-Y., Lu, Q., Fan, M., Yang, Y. & Posner, M. I. Mechanisms of white matter changes induced by meditation. *Proc. Natl Acad. Sci. USA* **109**, 10570–10574 (2012).
42. Newsome, W. T., Britten, K. H. & Movshon, J. A. Neuronal correlates of a perceptual decision. *Nature* **341**, 52–54 (1989).
43. Dienes, Z. How Bayes factors change scientific practice. *J. Math. Psychol.* **72**, 78–89 (2016).
44. De Schotten, M. T. et al. A lateralized brain network for visuospatial attention. *Nat. Neurosci.* **14**, 1245–1246 (2011).
45. Hayes, A. F. *PROCESS: A Versatile Computational Tool for Observed Variable Mediation, Moderation, and Conditional Process Modeling* White Paper. <https://api.semanticscholar.org/CorpusID:22220661> (2012).
46. Hayes, A. F. *Introduction to Mediation, Moderation, and Conditional Process Analysis: A Regression-Based Approach* (Guilford Press, 2013).
47. Fox, M. D., Corbetta, M., Snyder, A. Z., Vincent, J. L. & Raichle, M. E. Spontaneous neuronal activity distinguishes human dorsal and ventral attention systems. *Proc. Natl Acad. Sci. USA* **103**, 10046–10051 (2006).
48. Corbetta, M. & Shulman, G. L. Control of goal-directed and stimulus-driven attention in the brain. *Nat. Rev. Neurosci.* **3**, 215–229 (2002).
49. Vincent, J. L., Kahn, I., Snyder, A. Z., Raichle, M. E. & Buckner, R. L. Evidence for a frontoparietal control system revealed by intrinsic functional connectivity. *J. Neurophysiol.* **100**, 3328–3342 (2008).
50. Nelson, S. M. et al. A parcellation scheme for human left lateral parietal cortex. *Neuron* **67**, 156–170 (2010).
51. Grekes, C., Wang, L. E., Eickhoff, S. B. & Fink, G. R. Noradrenergic modulation of cortical networks engaged in visuomotor processing. *Cereb. Cortex* **20**, 783–797 (2010).
52. Corbetta, M., Patel, G. & Shulman, G. L. The reorienting system of the human brain: from environment to theory of mind. *Neuron* **58**, 306–324 (2008).
53. Corbetta, M. & Shulman, G. L. Spatial neglect and attention networks. *Annu. Rev. Neurosci.* **34**, 569–599 (2011).
54. Hanks, T. D. et al. Distinct relationships of parietal and prefrontal cortices to evidence accumulation. *Nature* **520**, 220–223 (2015).
55. O'Connell, R. G., Shadlen, M. N., Wong-Lin, K. & Kelly, S. P. Bridging neural and computational viewpoints on perceptual decision-making. *Trends Neurosci.* **41**, 838–852 (2018).
56. Romo, R. & de Lafuente, V. Conversion of sensory signals into perceptual decisions. *Prog. Neurobiol.* **103**, 41–75 (2013).
57. Shadlen, M. N. & Kiani, R. Decision making as a window on cognition. *Neuron* **80**, 791–806 (2013).
58. Assaf, Y., Johansen-Berg, H. & de Schotten, M. T. The role of diffusion MRI in neuroscience. *NMR Biomed.* **11**, e3762 (2017).
59. Johansen-Berg, H. Behavioural relevance of variation in white matter microstructure. *Curr. Opin. Neurol.* **23**, 351–358 (2010).
60. Kanai, R. & Rees, G. The structural basis of inter-individual differences in human behaviour and cognition. *Nat. Rev. Neurosci.* **12**, 231–242 (2011).
61. Zatorre, R. J., Fields, R. D. & Johansen-Berg, H. Plasticity in gray and white: neuroimaging changes in brain structure during learning. *Nat. Neurosci.* **15**, 528–536 (2012).
62. Hursh, J. B. Conduction velocity diameter of nerve fibers. *Am. J. Physiol.* **127**, 131–139 (1939).
63. Waxman, S. G. & Bennett, M. V. L. Relative conduction velocities of small myelinated and non-myelinated fibres in the central nervous system. *Nat. New Biol.* **238**, 217–219 (1972).
64. Selen, L. P. J., Shadlen, M. N. & Wolpert, D. M. Deliberation in the motor system: reflex gains track evolving evidence leading to a decision. *J. Neurosci.* **32**, 2276–2286 (2012).
65. Barbas, H. & Pandya, D. N. Architecture and frontal cortical connections of the premotor cortex (area 6) in the rhesus monkey. *J. Comp. Neurol.* **256**, 211–228 (1987).
66. Muakkassa, K. F. & Strick, P. L. Frontal lobe inputs to primate motor cortex: evidence for four somatotopically organized 'premotor' areas. *Brain Res.* **177**, 176–182 (1979).
67. Shushruth, S., Mazurek, M. & Shadlen, M. N. Comparison of decision-related signals in sensory and motor preparatory responses of neurons in area LIP. *J. Neurosci.* **38**, 6350–6365 (2018).
68. Wyart, V., Myers, N. E. & Summerfield, C. Neural mechanisms of human perceptual choice under focused and divided attention. *J. Neurosci.* **35**, 3485–3498 (2015).
69. Lortie, J. A. M. et al. The formation of hierarchical decisions in the visual cortex. *Neuron* **87**, 1344–1356 (2015).
70. Ditterich, J., Mazurek, M. E. & Shadlen, M. N. Microstimulation of visual cortex affects the speed of perceptual decisions. *Nat. Neurosci.* **6**, 891–898 (2003).
71. Gazzaley, A. & Nobre, A. C. Top-down modulation: bridging selective attention and working memory. *Trends Cogn. Sci.* **16**, 129–135 (2012).
72. Brosnan, M. B. et al. Prefrontal modulation of visual processing and sustained attention in aging, a transcranial direct current stimulation–electroencephalogram coregistration approach. *J. Cogn. Neurosci.* **30**, 1–16 (2018).
73. Twomey, D. M., Murphy, P. R., Kelly, S. P. & O'Connell, R. G. The classic P300 encodes a build-to-threshold decision variable. *Eur. J. Neurosci.* **42**, 1636–1643 (2015).
74. Hillyard, S. A., Squires, K. C., Bauer, J. W. & Science, P. L. Evoked potential correlates of auditory signal detection. *Science* **172**, 1357–1360 (1971).
75. Squires, K. C., Hillyard, S. A. & Lindsay, P. H. Vertex potentials evoked during auditory signal detection: relation to decision criteria. *Percept. Psychophys.* **14**, 265–272 (1973).
76. Sutton, S., Braren, M., Zubin, J. & John, E. R. Evoked-potential correlates of stimulus uncertainty. *Science* **150**, 1187–1188 (1965).
77. Courchesne, E., Hillyard, S. A. & Courchesne, R. Y. P3 waves to the discrimination of targets in homogeneous and heterogeneous stimulus sequences. *Psychophysiology* **14**, 590–597 (1977).
78. Johnson, C. C. D. & Donchin, E. On quantifying surprise: the variation of event-related potentials with subjective probability. *Psychophysiology* **14**, 456–467 (1977).
79. Polich, J. Updating P300: an integrative theory of P3a and P3b. *Clin. Neurophysiol.* **118**, 2128–2148 (2007).
80. Nieuwenhuis, S., Aston-Jones, G. & Cohen, J. D. Decision making, the P3, and the locus coeruleus–norepinephrine system. *Psychol. Bull.* **131**, 510–532 (2005).
81. Szurmi, B., Czobor, P., Komlósi, S. & Bitter, I. P300 deficits in adults with attention deficit hyperactivity disorder: a meta-analysis. *Psychol. Med.* **41**, 1529–1538 (2011).
82. Ford, J. M., Mathalon, D. H., Kalba, S., Marsh, L. & Pfefferbaum, A. N1 and P300 abnormalities in patients with schizophrenia, epilepsy, and epilepsy with schizophrenialike features. *Biol. Psychiatry* **49**, 848–860 (2001).
83. Frodl, T. et al. Value of event-related P300 subcomponents in the clinical diagnosis of mild cognitive impairment and Alzheimer's disease. *Psychophysiology* **39**, 175–181 (2002).
84. Ziegler, D. A. et al. Closed-loop digital meditation improves sustained attention in young adults. *Nat. Hum. Behav.* **3**, 746–757 (2019).
85. Storebø, O. J. et al. Methylphenidate for attention deficit hyperactivity disorder (ADHD) in children and adolescents. *Cochrane Database Syst. Rev.* <https://doi.org/10.1002/14651858.CD012069.pub2> (2012)
86. Loughnane, G. M. et al. Catecholamine modulation of evidence accumulation during perceptual decision formation: a randomized trial. *J. Cogn. Neurosci.* **31**, 1044–1053 (2019).
87. Chiang, M.-C. et al. Genetics of brain fiber architecture and intellectual performance. *J. Neurosci.* **29**, 2212–2224 (2009).
88. Newman, D. P., Loughnane, G. M., Kelly, S. P., O'Connell, R. G. & Bellgrove, M. A. Visuospatial asymmetries arise from differences in the onset time of perceptual evidence accumulation. *J. Neurosci.* **37**, 3378–3385 (2017).
89. Marshall, T. R., Bergmann, T. O. & Jensen, O. Frontoparietal structural connectivity mediates the top-down control of neuronal synchronization associated with selective attention. *PLoS Biol.* **13**, e1002272 (2015).
90. Chechlacz, M., Gillebert, C. R., Vangkilde, S. A., Petersen, A. & Humphreys, G. W. Structural variability within frontoparietal networks and individual differences in attentional functions: an approach using the theory of visual attention. *J. Neurosci.* **35**, 10647–10658 (2015).
91. Pelli, D. G. The VideoToolbox software for visual psychophysics: transforming numbers into movies. *Spatial Vis.* **10**, 437–442 (1997).
92. Brainard, D. H. The psychophysics toolbox. *Spat. Vis.* **10**, 433–436 (1997).
93. Cornelissen, F. W., Peters, E. M. & Palmer, J. The EyeLink Toolbox: eye tracking with MATLAB and the Psychophysics Toolbox. *Behav. Res. Methods Instrum. Comput.* **34**, 613–617 (2002).
94. Delorme, A. & Makeig, S. EEGLAB: an open source toolbox for analysis of single-trial EEG dynamics including independent component analysis. *J. Neurosci. Methods* **134**, 9–21 (2004).
95. Morel, P. Gramm: grammar of graphics plotting in Matlab. *J. Open. Source. Softw.* **3**, 568 (2018).
96. Kayser, J. & Tenke, C. E. Principal components analysis of Laplacian waveforms as a generic method for identifying ERP generator patterns: I. Evaluation with auditory oddball tasks. *Clin. Neurophysiol.* **117**, 348–368 (2006).
97. Foxe, J. J. & Simpson, G. V. Flow of activation from V1 to frontal cortex in humans. *Exp. Brain Res.* **142**, 139–150 (2002).

98. Kelly, S. P., Gomez-Ramirez, M. & Foxe, J. J. Spatial attention modulates initial afferent activity in human primary visual cortex. *Cereb. Cortex* **18**, 2629–2636 (2008).
99. Thut, G., Nietzel, A., Brandt, S. A. & Pascual-Leone, A. α -Band electroencephalographic activity over occipital cortex indexes visuospatial attention bias and predicts visual target detection. *J. Neurosci.* **26**, 9494–9502 (2006).
100. Andersson, J. L. R. & Sotiropoulos, S. N. An integrated approach to correction for off-resonance effects and subject movement in diffusion MR imaging. *NeuroImage* **125**, 1063–1078 (2016).
101. Jenkinson, M. & Smith, S. A global optimisation method for robust affine registration of brain images. *Med. Image. Anal.* **2**, 143–156 (2001).
102. Smith, R. E., Tournier, J.-D., Calamante, F. & Connelly, A. Anatomically-constrained tractography: improved diffusion MRI streamlines tractography through effective use of anatomical information. *NeuroImage* **62**, 1924–1938 (2012).
103. Power, J. D., Barnes, K. A., Snyder, A. Z., Schlaggar, B. L. & Petersen, S. E. Spurious but systematic correlations in functional connectivity MRI networks arise from subject motion. *NeuroImage* **59**, 2142–2154 (2012).
104. Ball, G. et al. Multimodal structural neuroimaging markers of brain development and ADHD symptoms. *Am. J. Psychiatry* **176**, 57–66 (2019).
105. D'Albis, M.-A. Local structural connectivity is associated with social cognition in autism spectrum disorder. *Brain* **141**, 3472–3481 (2018).
106. Esteban, O. et al. MRIQC: advancing the automatic prediction of image quality in MRI from unseen sites. *PLoS ONE* **12**, e0184661 (2017).
107. Griffanti, L. et al. ICA-based artefact removal and accelerated fMRI acquisition for improved resting state network imaging. *NeuroImage* **95**, 232–247 (2014).
108. Salimi-Khorshidi, G. et al. Automatic denoising of functional MRI data: combining independent component analysis and hierarchical fusion of classifiers. *NeuroImage* **90**, 449–468 (2014).
109. Boyacıoğlu, R., Schulz, J., Koopmans, P. J., Barth, M. & Norris, D. G. Improved sensitivity and specificity for resting state and task fMRI with multiband multi-echo EPI compared to multi-echo EPI at 7T. *NeuroImage* **119**, 352–361 (2015).
110. Griffanti, L. et al. Hand classification of fMRI ICA noise components. *NeuroImage* **154**, 188–205 (2017).
111. Parkes, L., Fulcher, B., Yücel, M. & Fornito, A. An evaluation of the efficacy, reliability, and sensitivity of motion correction strategies for resting-state functional MRI. *NeuroImage* **171**, 415–436 (2018).
112. Burgess, G. C. et al. Evaluation of denoising strategies to address motion-correlated artifacts in resting-state functional magnetic resonance imaging data from the human connectome project. *Brain Connect.* **6**, 669–680 (2016).
113. Ciric, R. et al. Benchmarking of participant-level confound regression strategies for the control of motion artifact in studies of functional connectivity. *NeuroImage* **154**, 174–187 (2017).
114. Power, J. D., Plitt, M., Laumann, T. O. & Martin, A. Sources and implications of whole-brain fMRI signals in humans. *NeuroImage* **146**, 609–625 (2017).
115. Fox, M. D., Zhang, D., Snyder, A. Z. & Raichle, M. E. The global signal and observed anticorrelated resting state brain networks. *J. Neurophysiol.* **101**, 3270–3283 (2009).
116. Saad, Z. S. et al. Trouble at rest: how correlation patterns and group differences become distorted after global signal regression. *Brain Connect.* **2**, 25–32 (2012).
117. Li, J. et al. Global signal regression strengthens association between resting-state functional connectivity and behavior. *NeuroImage* **196**, 126–141 (2019).
118. Satterthwaite, T. D. et al. An improved framework for confound regression and filtering for control of motion artifact in the preprocessing of resting-state functional connectivity data. *NeuroImage* **64**, 240–256 (2013).
119. Seeley, W. W. et al. Dissociable intrinsic connectivity networks for salience processing and executive control. *J. Neurosci.* **27**, 2349–2356 (2007).
120. Fox, M. D. et al. The human brain is intrinsically organized into dynamic, anticorrelated functional networks. *Proc. Natl Acad. Sci. USA* **102**, 9673–9678 (2005).
121. Dai, H. et al. Resting-state functional MRI: functional connectivity analysis of the visual cortex in primary open-angle glaucoma patients. *Hum. Brain Mapp.* **34**, 2455–2463 (2013).
122. Forstmann, B. U. et al. Cortico-subthalamic white matter tract strength predicts interindividual efficacy in stopping a motor response. *NeuroImage* **60**, 370–375 (2012).
123. Rouder, J. N. & Morey, R. D. The nature of psychological thresholds. *Psychol. Rev.* **116**, 655–660 (2009).
124. Baron, R. M. & Kenny, D. A. The moderator–mediator variable distinction in social psychological research: conceptual, strategic, and statistical considerations. *J. Pers. Soc. Psychol.* **51**, 1173–1182 (1986).

Acknowledgements

This work was supported by grants from the Australian Research Council (including DP150100986 and DP180102066) to M.A.B. and R.G.O. M.A.B. is supported by a Senior Research Fellowship from the Australian National Health and Medical Research Council (APP1154378). A.F. was supported by the Sylvia and Charles Viertel Foundation, National Health and Medical Research Council (1050504) and Australian Research Council (FT130100589). We thank N. Steinemann and D. McGovern for providing the additional data reported in Supplementary Results 1 and Supplementary Fig. 1, and J. Wiley and J. Matthews for statistical advice. The funders had no role in study design, data collection and analysis, decision to publish or preparation of the manuscript.

Author contributions

M.B.B., D.P.N., G.M.L., R.G.O. and M.A.B. conceived of the study. M.B.B., K.S., T.S., D.P.N., G.M.L., A.F., R.G.O. and M.A.B. developed the methodology. M.B.B., K.S., T.S., S.G., D.P.N. and G.M.L. developed the software. M.B.B., K.S. and T.S. performed the formal analysis. D.P.N. and G.M.L. performed the investigation. M.B.B. wrote the original draft of the manuscript. M.B.B., K.S., D.P.N., G.M.L., S.G., T.S., R.G.O. and M.A.B. reviewed and edited the manuscript. M.B.B. and T.S. visualized the data. A.F., R.G.O. and M.A.B. supervised the study. A.F., R.G.O. and M.A.B. acquired funding.

Competing interests

The authors declare no competing interests.

Additional information

Extended data is available for this paper at <https://doi.org/10.1038/s41562-020-0863-4>.

Supplementary information is available for this paper at <https://doi.org/10.1038/s41562-020-0863-4>.

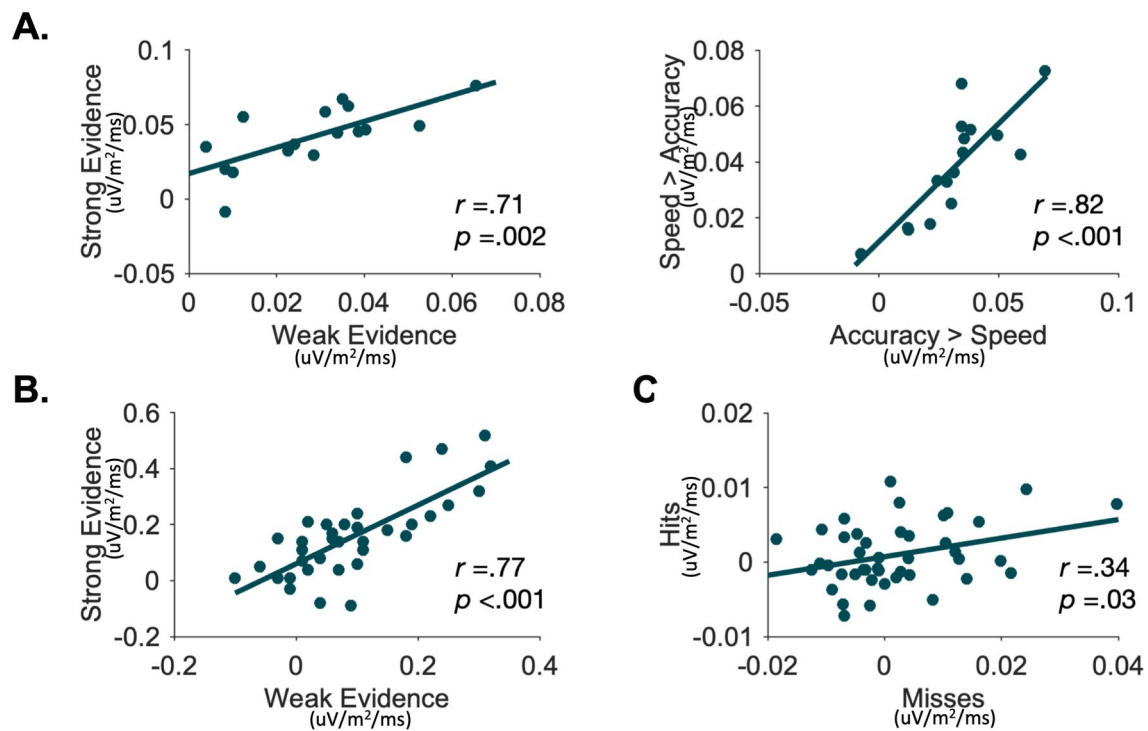
Correspondence and requests for materials should be addressed to M.B.B. or M.A.B.

Peer review information Primary Handling Editor: Marike Schiffer.

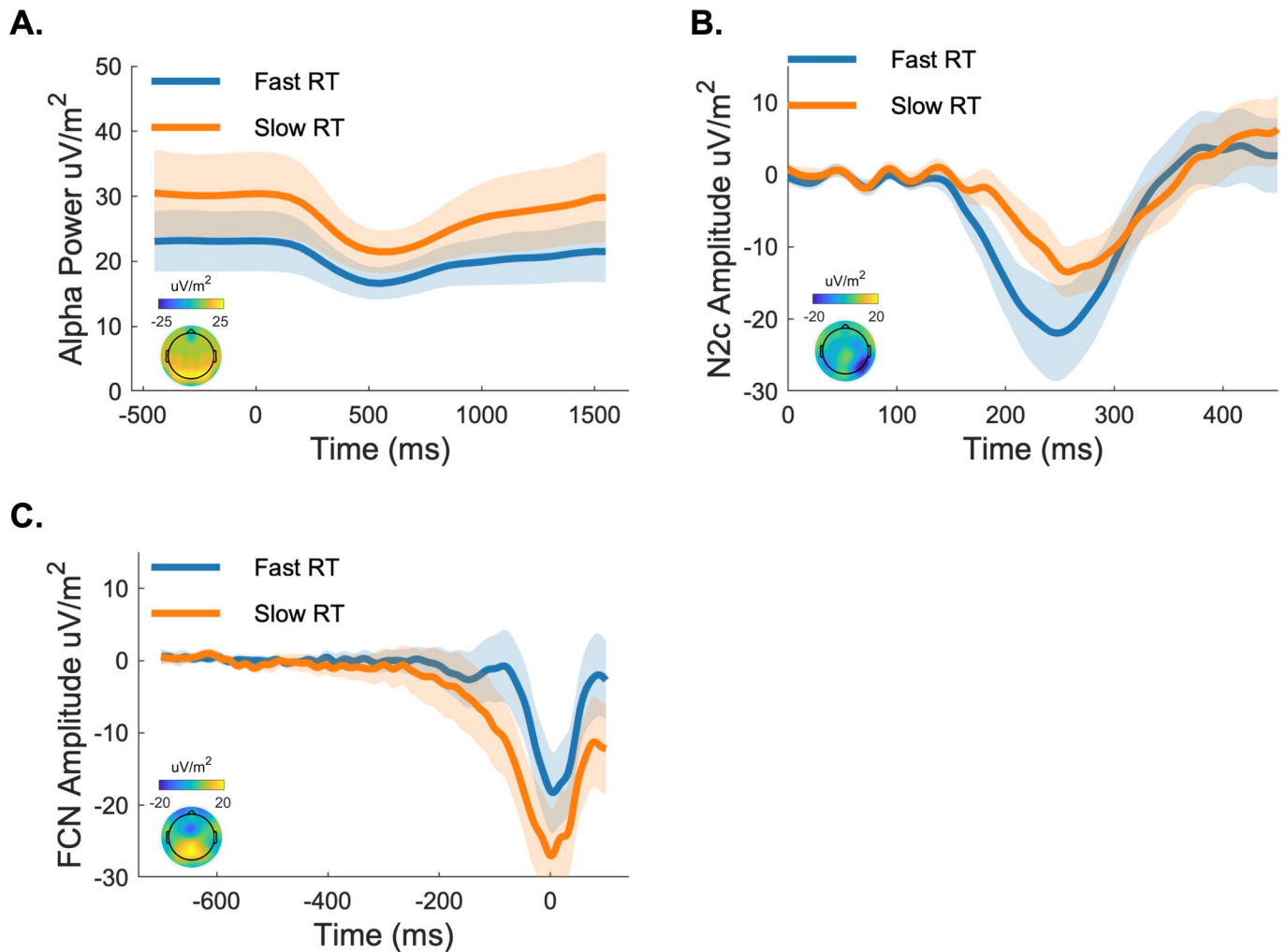
Reprints and permissions information is available at www.nature.com/reprints.

Publisher's note Springer Nature remains neutral with regard to jurisdictional claims in published maps and institutional affiliations.

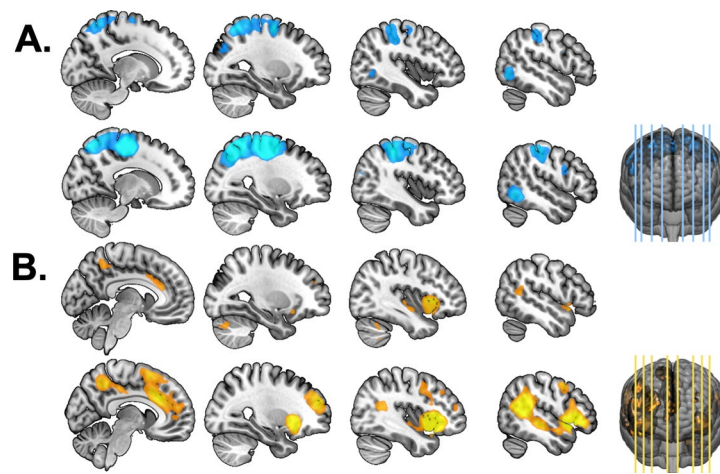
© The Author(s), under exclusive licence to Springer Nature Limited 2020



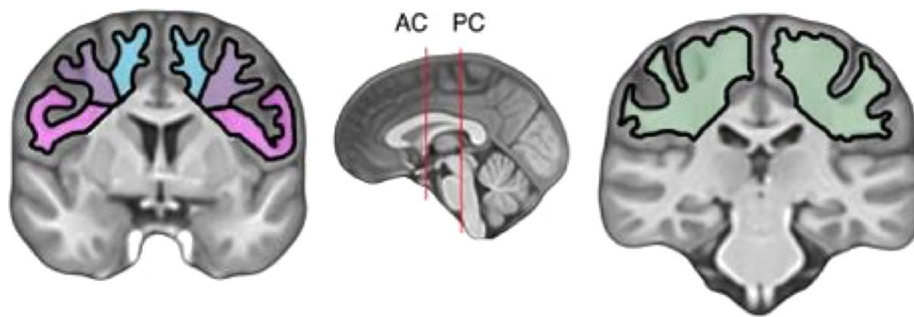
Extended Data Fig. 1 | Consistency of an individual's CPP build-up rate across experimental manipulations. **a**, Steinemann et al.²² *Nature Communications*. **b**, McGovern et al (2018) *Nature Human Behaviour*. **c**, Loughnane et al.²⁵ *Current Biology*. Note. For each sub-plot every data point depicts an individual's CPP build-up rate for condition a (as described on the x-axis), and condition b (as described on the y-axis). r denotes the correlation between the two experimental conditions using *Pearson's r*.



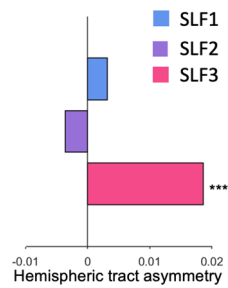
Extended Data Fig. 2 | EEG signals of relevance for RT but not accounting for independent variance. The EEG signals (pre-target alpha **a**, N2c (latency and amplitude) **b**, and FCN amplitude (**c**)) that offered a significant improvement in model fit for RT, over and above the signals that temporally preceded them but did not independently account for variance in RT. Please note data have been binned using a median split of participants' RT for visualisation purposes only. Given the window of interest is the pre-stimulus epoch, alpha power has not been baseline-corrected here (but see Supplementary Fig. 3).



Extended Data Fig. 3 | The dorsal and ventral FPN by hemisphere. The left and right hemispheres of the dFPN (**a**) and vFPN (**b**) respectively depicted in the upper and lower panels. *Note.* For the purpose of visualisation, these images were thresholded using a clusterwise FWE rate of $p < 0.001$ (extent threshold of 10 voxels).



Extended Data Fig. 4 | Regions of interest (ROI) used for the tractography of the three branches of the left and right superior longitudinal fasciculus on the cohort-specific T1 template. At the level of the AC, three ROIs delineate the superior (light blue), middle (purple) and inferior frontal gyri (pink) in each hemisphere. At the level of the PC is a single large parietal ROI (green).



Extended Data Fig. 5 | Lateralisation of the SLF. In line with previous work, the most ventral branch (SLF3) shows specific right lateralisation (Note, x-axis depicts right-left hemisphere volume, controlling for overall white matter volume, *** indicates $p < 0.0005$).

Reporting Summary

Nature Research wishes to improve the reproducibility of the work that we publish. This form provides structure for consistency and transparency in reporting. For further information on Nature Research policies, see [Authors & Referees](#) and the [Editorial Policy Checklist](#).

Statistics

For all statistical analyses, confirm that the following items are present in the figure legend, table legend, main text, or Methods section.

- | n/a | Confirmed |
|-------------------------------------|--|
| <input type="checkbox"/> | <input checked="" type="checkbox"/> The exact sample size (n) for each experimental group/condition, given as a discrete number and unit of measurement |
| <input type="checkbox"/> | <input checked="" type="checkbox"/> A statement on whether measurements were taken from distinct samples or whether the same sample was measured repeatedly |
| <input type="checkbox"/> | <input checked="" type="checkbox"/> The statistical test(s) used AND whether they are one- or two-sided
<i>Only common tests should be described solely by name; describe more complex techniques in the Methods section.</i> |
| <input type="checkbox"/> | <input checked="" type="checkbox"/> A description of all covariates tested |
| <input type="checkbox"/> | <input checked="" type="checkbox"/> A description of any assumptions or corrections, such as tests of normality and adjustment for multiple comparisons |
| <input type="checkbox"/> | <input checked="" type="checkbox"/> A full description of the statistical parameters including central tendency (e.g. means) or other basic estimates (e.g. regression coefficient) AND variation (e.g. standard deviation) or associated estimates of uncertainty (e.g. confidence intervals) |
| <input type="checkbox"/> | <input checked="" type="checkbox"/> For null hypothesis testing, the test statistic (e.g. F , t , r) with confidence intervals, effect sizes, degrees of freedom and P value noted
<i>Give P values as exact values whenever suitable.</i> |
| <input checked="" type="checkbox"/> | <input type="checkbox"/> For Bayesian analysis, information on the choice of priors and Markov chain Monte Carlo settings |
| <input type="checkbox"/> | <input checked="" type="checkbox"/> For hierarchical and complex designs, identification of the appropriate level for tests and full reporting of outcomes |
| <input type="checkbox"/> | <input checked="" type="checkbox"/> Estimates of effect sizes (e.g. Cohen's d , Pearson's r), indicating how they were calculated |

Our web collection on [statistics for biologists](#) contains articles on many of the points above.

Software and code

Policy information about [availability of computer code](#)

Data collection

The previously published perceptual decision making paradigm (see reference 68) was ran using MATLAB (MathWorks) and the Psychophysics Toolbox extensions (see references 69-71), while SR Research EyeLink eye tracker (Eye-Link version 2.04, SR Research/SMI) recorded eye movements.

Data analysis

All EEG preprocessing scripts implemented in the study are available at the following locations (https://github.com/gerontium/big_dots). These scripts are open access and available under a Creative Commons Attribution- NonCommercial-ShareAlike International License. Custom code for the resting-state MRI, and EEG data that support the conclusion of this article are available from the corresponding author upon request.

For manuscripts utilizing custom algorithms or software that are central to the research but not yet described in published literature, software must be made available to editors/reviewers. We strongly encourage code deposition in a community repository (e.g. GitHub). See the Nature Research [guidelines for submitting code & software](#) for further information.

Data

Policy information about [availability of data](#)

All manuscripts must include a [data availability statement](#). This statement should provide the following information, where applicable:

- Accession codes, unique identifiers, or web links for publicly available datasets
- A list of figures that have associated raw data
- A description of any restrictions on data availability

The EEG dataset from the current study is available at the following repository: <https://figshare.com/s/8d6f461834c47180a444>. This data is open access and available under a Creative Commons Attribution- NonCommercial-ShareAlike 3.0 International License. Raw data for the diffusion and resting-state imaging were collected at the Turner Institute for Brain and Mental Health as part of a large-scale project. Derived diffusion and resting-state MRI data supporting the findings of this study are available from the corresponding author upon request.

Field-specific reporting

Please select the one below that is the best fit for your research. If you are not sure, read the appropriate sections before making your selection.

☒ Life sciences ☐ Behavioural & social sciences ☐ Ecological, evolutionary & environmental sciences

For a reference copy of the document with all sections, see [nature.com/documents/nr-reporting-summary-flat.pdf](https://www.nature.com/documents/nr-reporting-summary-flat.pdf)

Life sciences study design

All studies must disclose on these points even when the disclosure is negative.

Sample size	Our sample consists of N=56 healthy younger individuals who, in addition to partaking in this EEG experiment, also participated in a larger imaging study (the Genetics of Cognition project, N=441). Recruitment for the EEG study was opportunistically conducted from the same participant database as the imaging study. As such, the sample size was not predetermined. Nonetheless, retrospective power calculations demonstrate that we have excellent power to detect our effects (>99% power for the behavioural-EEG findings; $\alpha=.05$, effect size $F^2=1.87$, N=56, 6 predictors; and 85.62% power for the CPP-SLF1 association, $\alpha=.05$, effect size $F^2=.21$, N=56, 2 predictors; G*Power 3.1)
Data exclusions	EEG trials were excluded from the analysis when particular conditions were met including pre-emptive behavioral responses, excessively high EEG signal indicative of an artifact, or if central fixation was broken (for further details see page 15). Four participants were excluded from resting state (rs) MRI investigation due to excessive in-scanner head motion resulting in a total sub-sample of N=52 individuals for these analyses. The threshold for excluding these individuals was determined relative to the distribution of a larger imaging sample (N=441; see page 19 for further details).
Replication	Our initial results, obtained by combining diffusion MRI with EEG, indicated that connectivity between dorsal but not ventral fronto-parietal network (FPN) regions accounted for individual differences in evidence accumulation build-up rate and, as a result, the speed of perceptual reports. To verify the reproducibility of these experimental findings we additionally examined whether resting state functional connectivity within these same networks underpinned variability in perceptual decision making. Consistent with our initial findings evidence accumulation rate was associated with stronger connectivity within the dorsal, but not ventral, FPN.
Randomization	Randomization was not relevant to our study as we did not conduct any experimental manipulations but rather investigated inter-individual differences in human behavior. Potential confounding factors which were not of interest in this study were included as covariates in all relevant analyses. Specifically these were age, gender, and overall white matter volume.
Blinding	Blinding was not relevant because participants in this study were not allocated to different groups.

Reporting for specific materials, systems and methods

We require information from authors about some types of materials, experimental systems and methods used in many studies. Here, indicate whether each material, system or method listed is relevant to your study. If you are not sure if a list item applies to your research, read the appropriate section before selecting a response.

Materials & experimental systems

n/a	Involved in the study
<input checked="" type="checkbox"/>	<input type="checkbox"/> Antibodies
<input checked="" type="checkbox"/>	<input type="checkbox"/> Eukaryotic cell lines
<input checked="" type="checkbox"/>	<input type="checkbox"/> Palaeontology
<input checked="" type="checkbox"/>	<input type="checkbox"/> Animals and other organisms
<input type="checkbox"/>	<input checked="" type="checkbox"/> Human research participants
<input checked="" type="checkbox"/>	<input type="checkbox"/> Clinical data

Methods

n/a	Involved in the study
<input checked="" type="checkbox"/>	<input type="checkbox"/> ChIP-seq
<input checked="" type="checkbox"/>	<input type="checkbox"/> Flow cytometry
<input type="checkbox"/>	<input checked="" type="checkbox"/> MRI-based neuroimaging

Human research participants

Policy information about [studies involving human research participants](#)

Population characteristics	See section entitled 'Randomization' above.
Recruitment	Participants for this study were recruited via advertising on both University and general social media platforms. Some participants heard about the study through word of mouth. We attempted to minimize self-selection bias in recruitment by advertising both within and outside the University media platforms.
Ethics oversight	The experimental protocol was approved by Monash University's human research ethics committee before testing and was carried out in accordance with the approved guidelines.

Note that full information on the approval of the study protocol must also be provided in the manuscript.

Magnetic resonance imaging

Experimental design

Design type	Resting State
Design specifications	One eyes-closed resting state block was obtained containing 620 functional volumes with 42 slices each using an interleaved acquisition
Behavioral performance measures	As this was a resting-state scan there were no behavioral performance measures.

Acquisition

Imaging type(s)	Functional, Structural, Diffusion
Field strength	3 Tesla
Sequence & imaging parameters	<p>Anatomical (T1) scan: magnetic-prepared rapid gradient echo sequence, field of view: 256 mm, matrix size: 240 x 256, slice thickness: 1mm, orientation: sagittal, TE: 2.07ms, TR:2300ms, flip angle: 9°.</p> <p>Diffusion scan: High-angular diffusion-weighted imaging , field of view: 240mm, matrix size: 96 x 96 , slice thickness: 2.5mm, orientation: axial, aligned through the ac-pc, TE: 100ms, TR:8800ms, flip angle: 90° ,</p> <p>Resting State functional scan: multiband echo-planar images (EPI), field of view: 190mm, matrix size: 64 x 64, slice thickness: 3mm, orientation: axial, aligned through the ac-pc, TE: 21ms, TR:754ms, flip angle:50°.</p>
Area of acquisition	Whole brain scans were acquired
Diffusion MRI	<input checked="" type="checkbox"/> Used <input type="checkbox"/> Not used
Parameters	60 directions, b-value of 3000 s/mm ² , single shell, no cardiac gating

Preprocessing

Preprocessing software	<p>Resting State Analysis: Initial preprocessing of EPI images was carried out using FSL FEAT, version 5.0.9, with the following procedure: removal of the first four volumes, rigid-body head motion correction, 3mm spatial smoothing to improve signal-to-noise ratio, and high-pass temporal filter of 75s. Subsequent spatial independent component analysis was performed using FSL MELODIC version 3.14. ICA components were used as inputs for FSL-FIX version 1.06 (11, 12), an ICA-based denoising approach that uses an automatic classifier to identify noise components and remove them from EPI data.</p> <p>Diffusion Analysis: Diffusion data were pre-processed using the MRtrix3 (version 0.3.15, https://github.com/MRtrix3) software package which included: denoising, motion, eddy current and susceptibility distortion correction⁷⁸, as well as bias field correction. A response function was estimated for each participant, followed by the generation of a fibre orientation distribution (FOD) map for each participant. In addition, tensor-derived fractional anisotropy (FA) scalar maps were generated.</p>
Normalization	<p>Resting State Analysis: Functional data were spatially normalized to the Montreal Neurological Institute (MNI) space using ANTs (version 2.2.0). Normalization was performed in a three-step method: 1) registration of the mean realigned functional scan to the skull-stripped anatomical T1 scan via a linear registration; 2) spatial normalization of the anatomical scan to the MNI template via a nonlinear registration; and 3) normalization of the functional scan to the MNI template using a transform from step 1 and 2 concatenated in a single transformation matrix.</p> <p>Diffusion Analysis: T1 images were registered to diffusion space using a linear registration⁷⁹. Subsequently, anatomically-constrained tractography (ACT) was performed in native space⁸⁰ to constrain whole brain tractography to the white matter/grey matter boundary. Constrained tractograms were generated using 2 million streamlines, seeding from the white/grey interface. The diffusion data were not transformed to standard space as we were not concatenating the data across groups. The tractography values generated in native space were extracted and used for further analyses, in relation the EEG data.</p>
Normalization template	<p>Resting State Analysis: Standardized space, MNI 152 nonlinear 6th generation template (see above)</p>

Diffusion Analysis:

T1 images were registered subject specific diffusion space. The data were not standardized (see above)

Noise and artifact removal**Resting State Analysis:**

Following basic preprocessing, spatial independent component analysis (ICA) was performed on the EPI data using FSL MELODIC version 3.14. The independent components were used as input into FSL-FIX (version 1.06), an ICA based denoising approach that utilizes an automated classifier to identify noise components and subsequently remove them from the data (82,83). The approach has been shown to efficiently remove motion and physiological noise, along with artifacts associated with multiband acceleration acquisition (82,84). We used a classifier that was trained on data from an independent sample of 25 individuals with the same scanner and acquisition parameters. Based on spatial characteristics, time-series fluctuations, and power spectra, we hand-trained the classifier by manually labeling over 2000 components as signal or noise (85).

Subsequently, the mean global signal from the entire brain was regressed from the data by taking the averaged signal from a whole-brain mask. We also removed the first derivative and squared signal and first derivative of the squared signal 86. This step has been shown to result in an optimal motion artifact removal following FSL-FIX87.

To control for movement artifacts during scanning, mean framewise displacement was used as an index of in-scanner head movement88. Mean framewise displacement (mFD) for each participant was estimated using the root mean squared volume-to-volume displacement of all voxels, derived from six head motion parameter estimates (3 translations, 3 rotations). Participants were excluded from analysis if their mFD exceeded 0.11mm. This threshold was determined by concatenating all participants' mFD values (from a larger imaging sample of 441 participants) into a single distribution and setting a threshold at the 75th percentile plus 1.5 times the interquartile range. This approach is similar to the 'fsl_motion_outliers' function of the FSL toolbox. Based on this value, participants were removed from further analysis using the following criteria: 1) their mean FD is greater than 0.11mm, 2) the sum of suprathreshold spikes is greater than 20%, or 3) if any FD is greater than 2.5mm (this value was adapted from previous work; see reference 89). The procedure resulted in the exclusion of 32 individuals from the larger sample.

Diffusion Analysis:

Pre-processing steps were carried out using MRtrix3 (version 0.3.15, <https://github.com/MRtrix3>) software package and included: denoising, motion, eddy current and susceptibility distortion correction78, as well as bias field correction

Volume censoring**Resting State Analysis:**

No volume censoring was performed for resting-state data.

However, poor quality scans were removed from subsequent analyses following quality check of data. Following acquisition, scans were checked for artifacts using MRIQC, an automated pipeline for quality checking of MRI scans81, as part of a larger imaging study (N=441 participants). Based on visual inspection of the reports, scans from nine people were removed from subsequent analyses due to artifacts or missing volumes.

Diffusion Analysis:

Volume censoring was not applicable for the diffusion analysis.

Statistical modeling & inference**Model type and settings****Resting State Analysis:**

Mass univariate. First- and second-level analyses were performed using SPM8 implemented in Matlab 2015b.r6685.

First-level analysis. To model the BOLD signal fluctuations in each voxel, for each participant, time-courses of each ROI were entered as a covariate into a general linear model. This step yields one whole-brain functional connectivity map for each ROI, leading to a total of four maps per participant that correspond to the IPF, FEF, TPJ, and VFC seeds.

Second-level analysis. To define the dorsal attention network, whole-brain voxelwise functional connectivity with the right IPS and the right FEF seeds was estimated. This was done by entering each participant's whole-brain functional connectivity maps of the right IPS and right FEF seeds from the first-level analysis into a random-effects second-level general linear model to generate a group-wide map of common regions that are functionally connected to the right IPS and FEF, thus comprising the dorsal attention network. The ventral attention network was delineated using a similar method by identifying common brain regions that are functionally connected with the TPJ and VFC seeds in a group-wide second-level general linear model. Refer to Table 4 for regions that are functionally connected with the FEF-IPS and TPJ-VFC.

To further test the specificity of our observed relationship between dFPN, but not vFPN functional connectivity and CPP build-up rate we delineated four additional networks: The Salience; Default Mode; Visual; and Basal Ganglia Networks, based on previously published seeds (respectively; see Supplementary Table 1).

Diffusion Analysis:

Model type and settings are not relevant for the diffusion analysis. The superior longitudinal fasciculus was dissected, as described in text, and the relevant parameters were extracted for further analysis.

Effect(s) tested**Resting State Analysis:**

There was no functional MRI task or stimulus conditions.

Diffusion Analysis:

This did not apply for the diffusion analysis. Please see above.

Specify type of analysis: ☐ Whole brain ☒ ROI-based ☐ Both

Anatomical location(s)

The dorsal and ventral attention networks were delineated using a seed-based analysis using in previously published work (see Fox et al., 2006, 31). Four regions of interest (ROIs; two dorsal, two ventral) were selected as a priori spherical seed ROIs (12mm3 radius), previously shown to correlate with resting-state fluctuations in networks resembling the dorsal and ventral attention network 31. The dorsal attention network ROIs included the right intraparietal sulcus (IPS; $x = 26$, $y = -62$, $z = 55$) and the right frontal eye field (FEF; $x = 23$, $y = -17$, $z = 56$). ROIs corresponding to the ventral attention network were seeded in the right temporal-parietal junction (TPJ; $x = 18$, $y = 38$, $z = 45$) and the right ventral frontal cortex (VFC; $x = 39$, $y = 21$, $z = -3$).

The Salience; Default Mode; Visual; and Basal Ganglia Networks, based on previously published seeds (respectively Right Orbital Frontotemporal, Posterior Cingulate/Precuneus, V1 (Primary Visual Cortex), Subthalamic Nucleus (STN))

Statistic type for inference

(See [Eklund et al. 2016](#))

Resting State Analysis:

Cluster-wise inference was used to determine significant regions. Parameters reported in text include peak MNI coordinates (x,y,z), Max T-Value, Cluster Extent (voxels), p value (cluster-wise FWE corrected).

Correction

For the resting-state analysis correction for multiple comparisons were conducted using a clusterwise family-wise error (FWE) rate of $p < .05$, with an initial cluster-forming threshold of $p < .001$ with a cluster extent of 10 voxels.

Diffusion Analysis:

We applied a Bonferroni multiple-comparison correction ($\alpha/12$) accounting for 12 statistical tests [2 EEG metrics (CPP build-up rate, LHB latency) by 3 SLF tracts (SLF1, SLF2, SLF3) by 2 tract measures (volume, FA)].

Exploratory Resting State Analyses:

For the exploratory analyses we applied Bonferroni-correction for multiple comparisons to account for 8 tests [2 EEG metrics (CPP build-up rate, LHB latency) by 4 resting state networks (Supplementary Table 1)].

For the hypothesis-driven confirmatory analyses (where we predicted that resting state connectivity in the dorsal but not ventral FPN would relate to CPP build-up rate), our results are uncorrected for multiple comparisons.

Models & analysis

n/a | Involved in the study

- ☐ ☒ Functional and/or effective connectivity
☒ ☐ Graph analysis
☒ ☐ Multivariate modeling or predictive analysis

Functional and/or effective connectivity

First-level analysis. In the within-subject first-level analysis, a general linear model was used to estimate the Pearson correlation between time-course signal of seed regions with every other voxel in the brain. A separate general linear model was used to estimate functional connectivity of each seed regions-of-interest (ROIs) (IPS, FEF, TPJ, and VFC) with the time-course of each ROI entered as a covariate in the model.

Second-level analysis. To assess the correlation between EEG and behavioural markers of perceptual decision making with whole-brain functional connectivity of the dorsal FPN, functional connectivity maps of whole-brain of IPS and FEF seeds were entered into a 2x1 factorial general linear model. The covariate of interest and nuisance covariates consisting of age, sex, and mean framewise displacement as a measure of in-scanner head motion were included in the model. The correlation between functional connectivity of the dorsal FPN with the variable of interest was estimated while controlling for the nuisance covariates. For each variable of interest, a separate model was estimated for the ventral FPN.